Vertical distribution of buoyant *Microcystis* blooms in a Lagrangian particle tracking model for short-term forecasts in Lake Erie

M. D. Rowe[1], E. J. Anderson[2], T. T. Wynne[3], R. P. Stumpf[3], D. L. Fanslow[2], K. Kijanka[1], H. A. Vanderploeg[2], J. R. Strickler[4], T. W. Davis[2]

[1] Correspondence to: University of Michigan, Cooperative Institute for Limnology and Ecosystem Research (CILER), NOAA Great Lakes Environmental Research Laboratory, 4840 S. State Rd., Ann Arbor, MI 48108-9719, phone 734-741-2172, fax 734-741-2055, mark.rowe@noaa.gov

[2] Great Lakes Environmental Research Laboratory, Oceanic and Atmospheric Research, National Oceanic and Atmospheric Administration, 4840 South State Road, Ann Arbor, MI 48108

[3] National Centers for Coastal Ocean Science, National Ocean Service, National Oceanic and Atmospheric Administration, 1305 East-West Highway, Silver Spring, MD 20910

[4] Great Lakes WATER Institute, University of Wisconsin – Milwaukee, 600 E. Greenfield Ave., Milwaukee, WI 53204-2944, USA

Key Points

Microcystis vertical distribution is a dynamic balance between turbulence and buoyancy

Appropriate time step and numerical scheme avoid artifacts in random walk models

Vertical mixing with buoyancy improved simulation of bloom spatial distribution

Abstract

Cyanobacterial harmful algal blooms (CHABs) are a problem in western Lake Erie, and in eutrophic fresh waters worldwide. Western Lake Erie is a large (3000 km^2), shallow (8 m mean depth), freshwater system. CHABs occur from July to October, when stratification is intermittent in response to wind and surface heating or cooling (polymictic). Existing forecast models give the present location and extent of CHABs from satellite imagery, then predict two-dimensional (surface) CHAB movement in response to meteorology. In this study, we simulated vertical distribution of buoyant *Microcystis* colonies, and 3D advection, using a Lagrangian particle model forced by currents and turbulent diffusivity from the Finite Volume Community Ocean Model (FVCOM). We estimated the frequency distribution of *Microcystis* colony buoyant velocity from measured size distributions and buoyant velocities. We evaluated several random-walk numerical schemes to efficiently minimize particle accumulation artifacts. We selected the Milstein scheme, with linear interpolation of the diffusivity profile in place of cubic splines, and varied the time step at each particle and step based on the curvature of the local diffusivity profile to ensure that the Visser time step criterion was satisfied. Inclusion of vertical mixing with buoyancy significantly improved model skill statistics compared to an advection-only model, and showed greater skill than a persistence forecast through simulation day 6, in a series of 26 hindcast simulations from 2011. The simulations and in-situ observations show the importance of

subtle thermal structure, typical of a polymictic lake, along with buoyancy in determining vertical and horizontal distribution of *Microcystis*.

Index Terms

4239 Limnology, 4842 Modeling, 4855 Plankton

Keywords

Numerical modeling, Ecological forecasting, Lake Erie, *Microcystis*, Harmful algal bloom, cyanobacteria

1 Introduction

Harmful algal blooms (HABs) are a global problem that is linked to anthropogenic eutrophication of inland and coastal waters, and may be exacerbated by climate change [*O'Neil, J. et al.*, 2012]. Lake Erie has experienced recurring blooms of toxin-producing cyanobacteria since the mid 1990s [*Brittain, S. M. et al.*, 2000; *Michalak, A. M. et al.*, 2013; *Wynne, T. T. and R. P. Stumpf*, 2015]. Lake Erie is the most productive, warm, and shallow of the Laurentian Great Lakes of North America. In the open waters of Lake Erie, cyanobacterial harmful algal blooms (CHABs) generally occur from July to October, and are dominated by the species *Microcystis aeruginosa*, which produces the group of hepatotoxin compounds known as microcystins [*Rinta-Kanto, J. M. et al.*, 2009]. CHABs occur primarily in the shallow western basin, which receives the main hydraulic load from the Detroit River in the north and the main nutrient load from the Maumee River [*Kane, D. D. et al.*, 2014] in the southwest (Fig. 1a). Occasionally, CHABs are transported

through the islands into the deeper central basin, while the eastern basin is largely free of CHABs (Fig. 1a)[*Wynne, T. T. and R. P. Stumpf*, 2015]. A bloom of record-breaking intensity and extent occurred in 2011. Analysis by Michalak et al. [2013] indicated that the conditions of meteorology and agricultural land use that caused the 2011 record bloom are likely to recur, and the 2015 bloom subsequently exceeded the severity of the 2011 record bloom [*Stumpf, R. P. and T. T. Wynne*, 2015].

Forecasts of CHAB abundance and spatial distribution are useful to water treatment plant operators, anglers, recreational boaters, and beach users. Lake Erie is a source of drinking water to 11 million people [*French, R. et al.*, 2011]. In 2014, the City of Toledo issued a do-not-drink order that affected a half million residents for two days as a result of contamination of treated water by microcystins [*Henry, T.*, 2014]. In addition to spatial forecasts, forecasts of *Microcystis* vertical distribution are of interest to water treatment plant operators because intake structures are usually located sub-surface, so the risk of toxins in their raw water may be greater during mixing events than when *Microcystis* colonies are concentrated on the surface. In addition to providing drinking water, Lake Erie supports economically valuable sport and commercial fisheries as well as recreation and tourism.

Short-term and seasonal CHAB forecasts have been developed for Lake Erie. Seasonal forecasts predict the annual bloom severity using statistical models based on the cumulative March to July phosphorus load from the Maumee River, which are able to explain > 90% of the interannual variance in bloom severity [*Obenour, D. R. et al.*, 2014]. Bloom severity is defined as the lake-wide cyanobacterial biomass averaged over the 30 days containing the maximum biomass

[*Obenour, D. R. et al.*, 2014; *Stumpf, R. P. et al.*, 2012], and has been estimated using both satellite [*Stumpf, R. P. et al.*, 2012] and plankton tow data [*Bridgeman, T. B. et al.*, 2013]. The seasonal forecast is used by water treatment plant managers for seasonal planning, to determine recommended phosphorus load reductions to meet commitments under the Great Lakes Water Quality Agreement [*GLWQA Annex 4*, 2015], and is distributed to over 1600 subscribers. Short-term forecasts are distinct from the seasonal forecast in the greater importance of physical transport processes over biological mechanisms in explaining short-term bloom variability. Experimental short-term forecasts have been developed for Lake Erie that indicate the present location and extent of CHABs from satellite imagery, then predict future movement of the CHAB using forecast meteorology, a hydrodynamic model, and a Lagrangian particle tracking model to simulate horizontal advection of neutrally-buoyant particles at the water surface [*Wynne, T. T. et al.*, 2013; *Wynne, T. T. et al.*, 2011].

Skill assessment of short-term CHAB forecasts is needed so that forecast users may have an appropriate level of confidence in forecast data, and for development of improved models. However, CHAB forecast skill assessment can be challenging, and methods are not well established. Wynne et al. [2011] showed that a forecast model more accurately predicted horizontal movement of the bloom centroid (center of mass) than a persistence forecast over a ten-day simulation for an August 2003 event. A persistence forecast is a benchmark used for model skill assessment in which no change is assumed from the initial observed location. The same quantitative skill assessment method could not be applied in the case of an August 2008 event because cloud cover and vertical mixing obscured parts of the bloom in subsequent images

and prevented an accurate estimate of the centroid location [*Wynne, T. T. et al.*, 2011]. In a detailed analysis of the August 2008 bloom in Lake Erie, Wynne et al. [2010] found that wind speed was a significant predictor of apparent bloom intensity in satellite imagery, and presented evidence to support the hypothesis that variation in the mixing depth of the buoyant cyanobacterial colonies was the underlying mechanism causing changes in surface concentration. In a qualitative analysis of the first three years of the experimental Lake Erie CHAB forecast (2008-2010), Wynne et al. [2013] concluded that the forecast provided useful information, but could be improved by a means to fill in cloud-covered areas in the satellite images, and by simulation of vertical mixing of the buoyant cyanobacteria.

To simulate concentration profiles of buoyant particles produced by vertical mixing in stratified turbulence, the partial differential equations governing advection and diffusion may be solved from an Eulerian or a Lagrangian perspective; each approach has strengths and weaknesses. Real phytoplankton communities have properties that vary among individuals within a population, such as size, specific gravity, light exposure history, and nutrient quotas. A strength of Lagrangian particle models is that nearly continuous distributions of properties can be represented by allowing properties to vary by particle [e.g., *Ross, O. N. and J. Sharples*, 2008], while in Eulerian models property distributions are usually represented by a limited number of discrete property classes [e.g., *Medrano, E. A. et al.*, 2013].

A weakness of the Lagrangian approach is that artificial accumulation of particles can occur in low diffusivity areas in random-walk turbulence simulations for the case of spatially (vertically) non-uniform diffusivity if an inappropriate numerical scheme or time step is used [*Visser, A.*,

1997]. These artifacts can be easy to misinterpret as features of interest. Several studies have applied Lagrangian particle models to the 1D column case with steady, idealized diffusivity profiles [*Gräwe, U. et al.*, 2012; *Ross, O. N. and J. Sharples*, 2008; *Visser, A.*, 1997]. In 3D ocean and lake models, use of random-walk vertical mixing schemes can be challenging because the required time step varies spatially and temporally over the model domain. A fixed time step may be selected that is adequate in most places and times [*Huret, M. et al.*, 2007], or in some cases a well-mixed profile was imposed in shallow regions where a small time step would be required to avoid formation of artifacts [*Gilbert, C. et al.*, 2010]. Our application required realistic rather than idealized diffusivity profiles for a polymictic lake in which conditions are alternately turbulent and stratified, and to simulate concentration profiles rather than specify a well-mixed condition, even in shallow areas, therefore some development of the random-walk approach was required.

We describe a short-term forecast system for CHAB abundance and distribution in Lake Erie that takes a similar approach to that of Wynne et al. [2011], but uses updated hydrodynamic and Lagrangian particle tracking models, and includes a means of filling in cloud-covered areas of satellite images using model data from a previous run. In addition, we describe a method to simulate vertical distribution of buoyant cyanobacteria in stratified turbulence. We evaluated the performance of several random-walk turbulence numerical schemes in terms of computational efficiency and their ability to minimize artifacts in simulations with vertically-varying diffusivity typical of a large polymictic lake. We compared simulated vertical distributions of cyanobacteria to observed profiles in Lake Erie. Finally, we show that model skill statistics were improved by

143 including vertical mixing with buoyancy in hindcast simulations of the spatial distribution of the
144 2011 bloom in Lake Erie.

145

146 ## 2 Methods

147 ### 2.1 Hydrodynamic model

148 The Finite Volume Community Ocean Model (FVCOM, v. 3.2) is an unstructured grid, finite-
149 volume, free surface, three-dimensional primitive equation ocean model that solves the
150 momentum, continuity, temperature, salinity, and density equations [*Chen, C. et al.*, 2003].
151 Turbulence closure is implemented through the MY-2.5 scheme for vertical mixing [*Galperin, B.*
152 *et al.*, 1988], and the Smagorinsky scheme for horizontal mixing [*Smagorinsky, J.*, 1963].
153 FVCOM has been adapted and implemented for the Great Lakes in several recent studies
154 [*Anderson, E. J. et al.*, 2015; *Anderson, E. J. and D. J. Schwab*, 2013; *Anderson, E. J. et al.*,
155 2010; *Bai, X. et al.*, 2013], yielding accurate predictions of temperature, water levels, and
156 currents. In particular, FVCOM has been applied to Lake Erie for extreme storm prediction
157 [*Anderson, E. J. et al.*, 2015] and serves as the oceanographic model underlying NOAA's next-
158 generation Lake Erie Operational Forecast System (LEOFS), a real-time short-term
159 hydrodynamic forecast model (http://tidesandcurrents.noaa.gov/ofs/leofs/leofs.html).

160 The FVCOM-based LEOFS model was applied for this study with bathymetry interpolated from
161 the NOAA National Geophysical Data Center.
162 (www.ngdc.noaa.gov/mgg/greatlakes/greatlakes.html). The unstructured grid consisted of 6,106

nodes and 11,509 elements (Fig. 1). Spatial resolution was 2 km in the central basin, 1.5 km in the western basin and 0.5 km in Maumee Bay and the islands (Fig. 1b) to improve representation of currents in these key areas for CHAB transport, with 20 uniform vertical sigma layers.

Dynamic water levels (6-minute) were prescribed at open boundaries at the Detroit River and the Niagara River, taken from adjustments to the NOAA/NOS gauges at Gibraltar (9044020) and Buffalo (9063020), to drive the primary inflow and outflow, respectively (Fig. 1a). Atmospheric forcing conditions were generated using station-based interpolation methods as in the NOAA Great Lakes Coastal Forecasting System (Beletsky et al., 2003; Schwab and Beletsky, 1998). Hourly meteorological forcing variables of wind speed, wind direction, air temperature, dewpoint temperature, and cloud cover were interpolated over Lake Erie from several land-based meteorological stations and offshore NOAA/NDBC buoys (45004, 45132, and 45142), when available. Wind speeds were adjusted to 10-m height and empirical relationships were used to adjust land-based meteorological variables for over-lake modification (Beletsky et al., 2003; Schwab and Beletsky, 1998).

Hydrodynamic model simulations were based on the real-time LEOFS nowcast, which was initialized on January 1, 2004 with uniform temperature of 2 $^{\circ}$C. For the 2011 scenario presented here, the hydrodynamic model simulation was initialized on January 1, 2011 with initial conditions provided by the simulation from the previous year, and produced hourly output of three-dimensional currents, water temperature, turbulent diffusivity, and 2D water level fluctuations.

2.2 Lagrangian particle tracking model

Lagrangian particle tracking was accomplished using a Fortran program developed previously to study transport of larval cod in the Gulf of Maine [*Churchill, J. H. et al.*, 2011; *Huret, M. et al.*, 2007], which is distributed as part of the FVCOM code package (http://fvcom.smast.umassd.edu/), and has previously been applied in the Great Lakes [*Anderson, E. J. and M. S. Phanikumar*, 2011]. Advection of particles was determined by

$$\frac{d}{dt}\boldsymbol{X}(t) = \boldsymbol{V}(\boldsymbol{X}(t), t) \tag{1}$$

where $\boldsymbol{X}(t)$ is the three-dimensional particle position at time t, and $\boldsymbol{V}(\boldsymbol{X}(t),t)$ is the three-dimensional, time varying velocity field. Linear interpolation in space and time was used to obtain $\boldsymbol{V}(\boldsymbol{X}(t),t)$ from hourly-archived FVCOM output. The contribution of advection to the particle position was updated by integrating Eq. (1) using an explicit fourth-order Runge-Kutta scheme with a time step, Δt = 600s. Vertical mixing due to turbulent eddy diffusivity was optionally simulated using one of several random-walk schemes, described below. We used reflected boundary conditions at vertical and horizontal boundaries in all simulations.

2.3 Well-mixed condition test

We compared the performance of several random walk vertical mixing numerical schemes using a well-mixed condition test case [*Visser, A.*, 1997] that can be used to evaluate whether a given numerical scheme and time step will produce artifacts in simulated concentration profiles. In our case, the well-mixed condition simulation was performed by initiating 1000 particles, uniformly distributed through the water column, then simulating 1D vertical mixing with neutral buoyancy

using time series of Lake Erie diffusivity profiles output from FVCOM for the month of August, 2011 (Table 1). Random noise in the simulated concentration profiles decreases with increasing number of particles, and 1000 particles were found to be adequate in 1D simulations [*Ross, O. N. and J. Sharples*, 2004]. These simulations are expected to give uniform concentration at all time regardless of the diffusivity profile, consistent with the Eulerian solution to the 1D diffusion equation with initial uniform concentration [*Visser, A.*, 1997].

To evaluate performance in the well-mixed condition test in a way that is directly relevant to our application, we defined a signal-to-noise ratio, *SN*, based on simulated surface concentration,

$$SN(t) = C(t)/|1.0 - C_{wm}(t)| \quad (2)$$

where $C_{wm}(t)$ is the time-dependent concentration in the 1-m thick surface layer, normalized to the column-mean concentration, in a well-mixed condition simulation with neutral buoyancy. A constant value of 1.0 is expected for $C_{wm}(t)$, therefore $|1.0 - C_{wm}(t)|$ represents the magnitude of "noise" due to artifacts and random fluctuations due to calculating concentration by counting discrete particles in a control volume. The "signal" is provided by the analogous surface concentration, $C(t)$, from an identical simulation *with* buoyancy. A large value of *SN* indicates that artifacts are small compared to the effect of interest, which is the fluctuation in surface concentration due to buoyancy. SN can be made arbitrarily large by using a small time step and a large number of particles, but at the expense of computational time. We selected a value of 5 as a goal minimum value for SN, based on the "Rose criterion" for the detection limit of the human eye for image features [*Rose, A.*, 1948]. Accordingly, we used the frequency of occurrence of SN

221 < 5 over the hourly records in a simulation as the performance criterion by which to evaluate the
222 numerical schemes and time step criteria.

223 2.4 Random walk vertical mixing schemes

224 We evaluated the Visser [1997] scheme, as-implemented by Huret et al. [2007]

$$z(t+\delta t) = z(t) + w_b \delta t + K'\big(z(t)\big)\delta t + R\sqrt{\frac{2K(\tilde{z})\delta t}{\sigma^2}} \tag{3}$$

225 where $z(t)$ is the vertical position of the particle at time t, δt is the vertical random walk time
226 step, w_b is a floating/sinking/swimming vertical velocity component, K is the vertical turbulent
227 diffusivity, $K' = dK/dz$, R is a random variable sampled from a uniform distribution with zero
228 mean and standard deviation σ, and $\tilde{z} = z(t) + 0.5K'(z(t))\delta t$ is a vertical position displaced
229 from the particle position as a function of the diffusivity gradient. Following Ross and Sharples
230 [2004], a cubic spline interpolation was used to obtain a continuous, differentiable diffusivity
231 profile.

232 In addition to the Visser scheme, described above, we evaluated random walk vertical mixing
233 schemes with higher order accuracy including the Milstein, Strong 1.5 (S1.5), and Platen two-
234 step (PC2) schemes that were implemented in Fortran for the General Ocean Turbulence Model
235 by Gräwe [2011]. After evaluating the performance of ten random walk schemes [*Gräwe, U.*,
236 2011], Grawe et al. [2012] recommended the use of either the Milstein scheme or higher-order
237 schemes such as S1.5 or PC2. The order of accuracy (rate of convergence) of numerical
238 approximations to stochastic differential equations is separated into weak and strong cases, where

239 the weak case relates to the accuracy of the ensemble particle distribution, while the strong case
240 relates to the accuracy of particle trajectories [*Gräwe, U.*, 2011]. The weak order of accuracy of
241 the schemes that we evaluated was 1 for Visser and Milstein, and 2 for S1.5 and PC2. The strong
242 order of accuracy was 1 for Milstein, 1.5 for S1.5, and was not defined for Visser or PC2 [*Gräwe,*
243 *U.*, 2011]. The Milstein scheme is

$$z(t+\delta t) = z(t) + w_b \delta t + 0.5K'\big(z(t)\big)[\Delta \mathrm{W}^2 + \delta t] + \Delta W\sqrt{2K(z(t))} \tag{4}$$

244 where ΔW is a random variable drawn from a Gaussian distribution with zero mean and standard
245 deviation $\sqrt{\delta t}$. Because the Milstein scheme is first order, linear interpolation of the diffusivity
246 profile to obtain $K(z(t))$ and $K'\big(z(t)\big)$ are sufficient, and the added computational expense
247 compared to the Visser scheme (Eq. 3) is minimal. The second order schemes S1.5 and PC2
248 retain additional terms from the stochastic Taylor expansion, including higher order derivatives
249 that require the application of cubic splines to the diffusivity profile, and S1.5 requires an
250 additional random variable, therefore the second order schemes have greater computational
251 expense. We refer to Gräwe [2011] for a full explanation of the S1.5 and PC2 schemes.

252 ## 2.5 Random walk time step

253 Visser [1997] introduced a time step criterion, $\delta t \ll \min(1/|K''|)$, where K'' is the second
254 derivative of the diffusivity profile, so that the diffusivity profile is reasonably approximated by a
255 first-order Taylor series expansion over the range of particle displacement. Ross and Sharples
256 [2004] found that

$$\delta t = \frac{1}{100|K''|} \tag{5}$$

is acceptable in most applications. To ensure the use of an appropriate time step throughout a 3D model domain, and to avoid the need to specify an appropriate δt in advance, we modified the code of Huret et al. [2007] to allow an appropriate value of δt to be calculated and applied for each particle at each δt. To evaluate Eq. (5) independently of spline interpolation, we calculated K'' directly at the FVCOM sigma levels using a centered finite difference approximation, and extended the profile beyond the surface and bottom by reflection. We further limited $0.01\ s \leq \delta t \geq \Delta t$. We tracked the minimum δt during simulations to confirm that the lower limit of 0.01 seconds was rarely applied.

2.6 Measurement of *Microcystis* colony size distribution

We assigned buoyant velocity in the model based on measured size distributions and regressions of buoyant velocity versus colony diameter. We measured *Microcystis* colony diameter of Lugol preserved samples collected from western Lake Erie in the summers of 2012, 2013, and 2014. In 2012 and 2013 colony diameters were measured by microscopy (Table 1). In 2014 we used the FlowCam (Fluid Imaging Technologies). The FlowCam captures images of individual colonies and estimates their equivalent spherical diameter by image analysis. Wang et al. [2015] showed that counts and colony diameters of *Microcystis* given by FlowCAM and microscopic image analysis diameters were nearly identical. Colonies in Lake Erie are typically > 50 μm [*Vanderploeg, H. A. et al.*, 2001] and buoyant. Samples were preserved with 1% formalin upon collection, immediately refrigerated, and analyzed within 24 hours. FlowCam analyses were

performed with a 2× objective and 1 × 3 mm field of view flow cell with samples diluted as per manufacturer recommendations to avoid capturing more than one image per trigger event. Fluorescent triggering mode was used to avoid imaging detrital material that might be confused with *Microcystis*. Samples were diluted in 0.2 μm filtered algal culture media [e.g., *Vanderploeg, H. A. et al.*, 2001] and injected into the FlowCAM with a 60-mL syringe, which was constantly turned over so as to prevent the buoyant colonies from aggregating in the syringe. The image analysis algorithm was calibrated to identify the colony outline including the mucilage.

2.7 Measurement of *Microcystis* colony buoyant velocity

Microcystis colony buoyant velocity was measured using microscopic videography [*Bundy, M. H. et al.*, 1998; *Strickler, J. R.*, 1985], a method in principle similar to that of Nakamura et al. [1993]. Surface water samples were collected on 15 and 21 July 2015 (Table 1) at station WE15 (Fig. 1b, -83.0, 41.6) during the early afternoon. Water was placed in 1-L glass bottles in an incubator outdoors with a neutral density filter to cut light intensity to 50% of surface irradiance. Measurements of colony velocities were made throughout the morning and afternoon of the next day. Digital video clips were captured of individual colonies rising through a 2-cm × 2-cm cross section × 30-cm tall glass cuvette filled with ambient lake water inside of a water jacket in a temperature controlled environmental room maintained at the lake temperature. Image capture and analysis software (Templo Motus, Vicon Motus, Contemplas, GmbH, Germany) was used to measure the velocity of the rising colonies. Diameters of the colonies were determined from image analysis of video images using Image-Pro software (Media Cybernetics, Rockville, MD).

296 Water samples were diluted as needed with 0.2- μm filtered lake water to avoid turbulence
297 induced by multiple rising colonies.

298 2.8 Measured vertical profiles of temperature and cyanobacterial concentration

299 Vertical profiles of temperature and cyanobacterial concentration (reported in μg chlorophyll a L^{-1}
300) were measured using the FluoroProbe (bbe Moldaenke, GmbH), which uses spectral
301 fluorometry to partition total chlorophyll into multiple phytoplankton classes on the basis of their
302 characteristic pigments (green algae, cyanobacteria, diatoms/dinoflagellates, cryptophytes), with
303 correction for possible interference by colored dissolved organic matter [*Catherine, A. et al.*,
304 2012; *Kring, S. A. et al.*, 2014]. Standard factory calibration settings for representative algal
305 classes were used. Profiles were measured at 11 stations (Fig. 1) weekly from June through
306 September, 2015 (Table 1). Profiles were selected for model skill assessment in which the
307 cyanobacterial chlorophyll was greater than chlorophyll from other algal classes, which occurred
308 13 July to 28 September.

309 2.9 Satellite remote sensing data

310 To initialize model simulations, and for model skill assessment, we used a series of images of
311 cyanobacterial blooms in Lake Erie from July to October 2011 (Table 1) that were derived from
312 the Medium Resolution Imaging Spectrometer (MERIS) [*Wynne, T. T. and R. P. Stumpf*, 2015].
313 MERIS standard level 2 data sets (in units of sr^{-1}) were used with a spectral shape algorithm
314 based around 680 nm [*Wynne, T. et al.*, 2008] to obtain the cyanobacterial index (CI). CI varies
315 linearly with biomass, with a value of 10^{-3} sr^{-1} corresponding to approximately 10^5 cells mL^{-1}

316 [*Stumpf, R. P. et al.*, 2012], which is the World Health Organization's threshold of significantly
317 increased risk for human health effects [*Chorus, I. and J. Bartram*, 1999]. For our analysis, we
318 converted CI to chlorophyll concentration using an empirical relationship derived from field
319 radiometry and grab sample extracted chlorophyll from eutrophic lakes in Florida (R^2 0.95, std.
320 error 7.7 µg L^{-1}, range 16 to 115 µg L^{-1}). The relationship was also verified for satellite-derived
321 CI, and gave a relative root-mean square error of 27% [*Tomlinson, M. C. et al.*, 2016].

$$Chl = 12570\ CI + 10 \tag{6}$$

322 A value of CI = 10^{-3} sr^{-1} is approximately equivalent to 23 µg L^{-1} chlorophyll, which we used as a
323 threshold to define the presence of a CHAB.

324 2.10 Hindcast simulations

325 Daily satellite images for the period July to October 2011 were evaluated, and 26 images were
326 selected that had > 50% cloud-free views of western Lake Erie. A ten-day model simulation was
327 initialized from each image by assigning surface chlorophyll concentration values to FVCOM
328 nodes by nearest neighbor interpolation. Concentration was converted to Lagrangian particles by
329 specifying a chlorophyll mass per particle (10^{10} µg Chl $particle^{-1}$) and placing the specified
330 number of particles within a control volume. The FVCOM node-centered tracer control elements
331 were used as control volumes (Fig. 1). Vertical layers were specified as constant-thickness (1 m)
332 z-layers.

333 Preliminary hindcast skill assessment indicated a need to censor satellite data within a buffer
334 region of shorelines due to frequent false positives in these areas, which was likely caused by

contamination of the water signal from relatively bright surrounding land or by bottom reflectance. The buffer width was set to 1 km south of Stony Point (41.94 °Lat.) and east of Catawba Island (-82.85 °Lon.) and to 1.5 km elsewhere. The buffer was not applied in Maumee Bay because CHABs were often present [*Wynne, T. T. and R. P. Stumpf*, 2015], reducing the likelihood of false positives. Buffered or missing data areas were assigned values by nearest neighbor if pixels containing valid data were available within 2 km. If no valid pixels were available within 2 km of a node one of two approaches was used: 1) it was assumed that no CHAB was present ($Chl = 0$), or 2) model output was carried forward to fill in the no-data area if a previous model run was available covering the time period.

Two types of simulations were run, 2D and 3D. In 2D simulations, the surface chlorophyll concentration was applied to the surface 1 m, with $Chl = 0$ below, and random walk vertical mixing was turned off. In 3D simulations, surface chlorophyll concentration was applied over the surface mixed layer (SML) depth (see below), and random walk vertical mixing was simulated. Both 2D and 3D simulations included 3D advection.

2.11 Estimation of the surface mixed layer depth

It was necessary to estimate the surface mixed layer (SML) depth for buoyant *Microcystis* colonies for the purpose of initializing the vertical distribution of particles (chlorophyll concentration) in 3D simulations from satellite-derived surface chlorophyll concentration. The vertical distribution of buoyant particles in the water column depends on buoyancy in addition to turbulent diffusivity (e.g., Fig. 2d,e); therefore, we used the Lagrangian particle model to estimate the initial vertical distribution of *Microcystis* colonies rather than using diffusivity or temperature

356 profiles from FVCOM directly. Initial vertical profiles were simulated at a subset of FVCOM
357 nodes (stations) because a large number of particles is needed to obtain a well-resolved profile,
358 which would be computationally intensive to simulate at all 6,106 nodes. The SML depth was
359 estimated by running 1D column vertical random walk simulations at 11 station locations (Fig.
360 1b) that were selected to provide representative coverage of the western basin where CHABs are
361 most common, with additional stations added at representative deeper locations. 1D simulations
362 were initialized with 1000 particles uniformly distributed over the column 36 hours prior to the
363 initialization time of the 3D model (satellite image time) to allow the particle distribution
364 sufficient time to adapt to the varying diffusivity. Random walk vertical mixing was forced by
365 hourly diffusivity output from FVCOM. The SML depth for *Microcystis* colonies was estimated
366 as the depth at which the 1D concentration profile decreased to half the surface concentration,
367 and the satellite-derived surface concentration was applied from the surface to this depth; this
368 approach provides an unbiased estimate of the total column biomass for the case of a uniform
369 concentration profile or a profile that can be approximated by a linear decrease. SML depth was
370 interpolated spatially to the FVCOM nodes by the nearest neighbor method.

371 ## 2.12 Model skill statistics

372 Comparison of model results to in-situ profile data was conducted using column-integrated
373 quantities to minimize the effect of noise in the profile data on the statistics. Turbulent diffusivity
374 is strongly influenced by the static stability of the water column, which can be quantified using
375 the potential energy anomaly, ϕ,

$$\phi = \frac{1}{h}\int_0^h (\hat{\rho} - \rho) g z dz \,;\;\; \hat{\rho} = \frac{1}{h}\int_0^h \rho dz \tag{7}$$

where ρ is the local density, h is the water column depth, and g is acceleration due to gravity [*Simpson, J. and D. Bowers*, 1981; *Wiles, P. et al.*, 2006]. Vertical distribution of concentration was characterized by calculating the center of mass of the normalized concentration profile, σ_m

$$\sigma_m = \frac{1}{C}\sum_{k=1}^{k_b} c_k \sigma_k \,;\; C = \sum_{k=1}^{k_b} c_k \tag{8}$$

where $\sigma = z/h$ is the normalized vertical coordinate, c is the concentration at layer k normalized to the column-mean concentration, $k_b = 20$ is the number of uniformly-spaced σ layers in the model grid. The observed concentration profile was averaged over the σ layers of the model grid for the purpose of comparison to the model profiles.

Skill assessment in hindcast simulations was conducted by comparing model results to remote sensing images that were within the model simulation period. Each hindcast simulation was initialized from a satellite image, and two to four subsequent images were typically available within the simulation period for skill assessment. Skill assessment was conducted using a binary categorical variable (CHAB, no CHAB), and pixel-by-pixel comparisons of model to remote sensing observations were conducted. FVCOM tracer control elements (Fig. 1) were used as the spatial segmentation (pixels).

Our approach to skill assessment statistics followed Hogan and Mason [2012]. Two statistics were calculated from the elements of the contingency table, which are the number of *a*, correctly

predicted events (hits); *b*, false events (false alarms); *c*, false negatives (misses); and *d*, correct non-events. The frequency bias (B) gives the ratio of the number of forecasts of occurrence to the number of observed occurrences,

$$B = \frac{a+b}{a+c} \tag{9}$$

and the Pierce Skill Score (PSS) gives the hit rate minus the false alarm rate.

$$PSS = \frac{ad-bc}{(b+d)(a+c)} \tag{10}$$

An unbiased forecast has a frequency bias B = 1.0. PSS values range from -1.0 to 1.0, with positive values indicating that the hit rate was greater than the false positive rate, and therefore the model had greater skill than a random forecast or constant CHAB or no-CHAB prediction [*Hogan, R. J. and I. B. Mason*, 2012].

To provide a reference forecast for skill comparison, we defined a "persistence" forecast as the assumption of no change from the satellite image that was used to initialize the model, which represents the best available information to a forecast user in the absence of a useful model. We took the further steps of filling in missing data in the persistence forecast with the most recent satellite data for each spatial segment, and applying the same shoreline buffering procedure that was used to initialize the model.

To test whether the model had significantly greater skill than the persistence forecast, we used the bootstrap method described by Hogan and Mason [2012] to estimate the confidence interval around the difference in skill score of the model compared to the persistence forecast. Starting

409 with a series of *n* triplets of observations, model predictions, and persistence predictions, we
410 created 1000 different bootstrap samples, each of length *n*, by taking random samples with
411 replacement from the series. We then calculated the difference in *PSS*, *ΔPSS*, for each bootstrap
412 sample. Finally, we estimated the 95% confidence interval as the 0.025 to 0.975 quantiles of the
413 ensemble of 1000 values of *ΔPSS*. While analytical formulas are available to estimate the
414 uncertainty in PSS, the bootstrap method accounts for effects of spatial and temporal
415 autocorrelation in environmental data, which effectively reduce the number of independent
416 observations to be < *n* [*Hogan, R. J. and I. B. Mason*, 2012].

417

418 ## 3 Results and Discussion

419 Western Lake Erie is polymictic, meaning that it does not continuously stratify during the
420 summer owing to shallow bathymetry and exposure to wind. Temperature profiles simulated by
421 FVCOM show periods of temporary stratification that are strongest during calm afternoons when
422 the surface is warmed by the sun and warm summer air (Figure 2a, 19-20 Aug.). At night,
423 cooling of the surface often causes deepening of the surface mixed layer by convection. This diel
424 cycle can be overpowered by shear-induced mixing during windy periods (Fig. 2a, 21-22 Aug.).
425 The temperature difference over the water column during periods of stratification is small (Fig.
426 2a), but the static stability is sufficient to cause turbulent diffusivity to vary by orders of
427 magnitude over a depth range of a few meters (Fig. 2b). Random walk turbulence schemes are
428 susceptible to formation of artificial accumulations of particles in the presence of strong gradients
429 in diffusivity [*Visser, A.*, 1997].

3.1 Vertical random walk schemes

We tested the random walk schemes using a 1D well-mixed condition simulation (see Methods) that was run using hourly time series of diffusivity profiles output from FVCOM for the month of August 2011 at stations representative of the range of conditions that occur during the summer CHAB season in western Lake Erie (Fig. 1). The range of conditions represented by the diffusivity profiles can be characterized by defining a Peclet number that represents the ratio of mixing time scale to floating/sinking time scale of the water column, $Pe = w_b h/\overline{K}$, where h is the water column depth and $\overline{K}$ is the column mean eddy diffusivity [*Ross, O. N. and J. Sharples*, 2004]. Values of $Pe >> 1$ indicate that w_b has a strong influence on particle concentration profiles. Combining the time series of diffusivity profiles that was used in the well-mixed condition simulations with $w_b = 70$ μm s^{-1} (see below), values ranged on the order of $0.01 < Pe < 100$. A small time step is usually required for $Pe << 1$ because small h and large $\overline{K}$ will produce strong gradients in diffusivity for realistic diffusivity profiles (i.e., $K \sim 0$ at the bottom or at the thermocline), and therefore, small values of the Visser time step criterion (Eq. 3). At the 3-m deep station (WE6) the variable time step occasionally was limited by the specified minimum and maximum values of 0.01 and 600 s, with typical hourly means of 0.2-3 s. At the 13-m deep station (NDBC45005) in the central basin the water column was continuously stratified, and longer time steps could be used; hourly minimum values of the variable time step were typically 0.2-2 s, mean values were 3-30 s and maximum hourly values were constrained by the upper limit of 600 s.

Example time series of concentration profiles output from a well-mixed condition simulation are shown in Figure 2. A typical particle accumulation artifact is visible in Fig. 2c, where the normalized concentration deviated from the expected constant value of unity. The artifact formed when high diffusivity in the surface mixed layer on 24 August (Fig. 2b) caused particles to jump across the sharp diffusivity gradient into the area of low diffusivity in the lower half of the water column without the opportunity for the gradient term (Eq. 3-4) to push the particles back toward the high diffusivity SML. Improved performance can be seen in Fig. 2d, where the variable time step was reduced during the high diffusivity event on 24 August, thereby limiting the maximum particle displacements and reducing the magnitude of the artifact.

The Gräwe Milstein scheme [*Gräwe, U.*, 2011] with the variable time step provided the best combination of computational efficiency and accuracy of the random-walk numerical schemes tested. The shortest run time was achieved by the Gräwe Milstein scheme (Fig. 3a), which was unique in the use of linear interpolation of diffusivity to the particle position, while the other schemes used cubic splines at a greater computational cost. The second order schemes, PC2 and S1.5, required greater computational effort to calculate additional terms and had the longest run times. The run time of the variable time step simulation was similar to that of the fixed 1 s time step for the Visser and Milstein schemes because the average of the variable time step was similar to the value of the fixed 1 s time step (Fig. 3a). The Milstein schemes showed improved accuracy compared to the Visser scheme with the fixed 1 s time step (Fig. 3b), consistent with the finding of Gräwe [2011]. All schemes were more accurate with the variable time step than with the fixed 1 s time step (Fig. 3b) because the Visser time step criterion (Eq. 5) was always

satisfied in the case of the variable time step. The second order schemes did not offer sufficiently improved accuracy to compensate for their greater computational effort (Fig. 3a,b).

In contrast to our result, Gräwe (2011) found that the second order schemes did offer improved accuracy that justified the additional computational effort, but for the case of idealized diffusivity profiles specified at high vertical resolution and for a realistic test case of a tidally-mixed bay with model diffusivity output at 200 levels. In our case of a shallow polymictic lake, diffusivity profiles were highly irregular with sharp gradients (Fig. 2b), and diffusivity was output at only 20 levels. We found that spline fits often had spurious features between the levels at which diffusivity was specified by FVCOM that were not representative of physically realistic diffusivity profiles. Higher-order random walk schemes depend on higher-order derivative terms from the spline fits to the diffusivity profiles [*Gräwe, U.*, 2011], which may not be accurate in the case of a non-representative spline fit. The higher order schemes might produce better results if we were to output diffusivity at a large number of levels, but that would come at the expense of greater computational effort in the hydrodynamic model. For our application, the Gräwe Milstein scheme produced satisfactory results and did not require a spline fit, so it was selected for further work.

3.2 *Microcystis* colony size distribution and buoyant velocity

The parameter w_b represents the *Microcystis* colony terminal velocity resulting from the balance of forces between buoyancy and fluid drag. Our approach was to specify a *Microcystis* colony size distribution, then apply an empirical relationship between w_b and colony diameter to obtain a frequency distribution of w_b for use in the model. According to Stoke's law for the terminal

492 velocity of a floating/sinking spherical particle in a fluid, one might expect the relationship
493 between w_b and colony diameter to give a straight line on a log-log plot with a slope of 2.
494 However, Nakamura et al. [1993] showed that *Microcystis* colony specific gravity approaches
495 that of the surrounding fluid as colony diameter increases owing to the fractal geometry of the
496 colonies and the increasing volume of void spaces filled with the surrounding water; the result is
497 that the slope of the log-log plot is < 2.

498 The *Microcystis* colony diameter frequency distribution measured by FlowCam was unimodal
499 with a median of 117 μm and a maximum of 740 μm (Fig. 4a, Station WE12, 4 Aug 2014). The
500 size frequency distribution measured by microscopy on samples collected at stations WE 2,4,6,
501 and 8 in July – October 2013 and June – July 2014 gave a similar size distribution to that of the 4
502 August 2014 sample (Fig. 4a). It is likely that the colony size distribution varies to some extent
503 spatially and temporally [e.g., *Lin, L. et al.*, 2014], and our estimate could be refined through
504 additional measurements. Even so, the consistency between our two estimated size distributions
505 gives some indication of representativeness.

506 Our measured values of Lake Erie *Microcystis* colony buoyant velocity, w_b, were similar to those
507 of Nakamura et al. [1993] for colonies larger than 200 μm in their sample collected from a lake in
508 Japan on 3 August 1990, and generally less than their 18 September sample (Fig. 4b). We were
509 not able to resolve colonies smaller than 200 μm by our method; however, large colonies account
510 for the majority of biomass and toxin concentration. For example, colonies > 112 μm accounted
511 for 93% of *Microcystis* cells (biomass) in Lake Erie samples [*Chaffin, J. D. et al.*, 2011], and
512 colonies > 100 μm showed the highest proportion of microcystin-producing genotypes, highest

513 microcystin cell quotas, and highest microcystin production rate, compared to smaller colony size
514 classes in Lake Wannsee, Germany [*Kurmayer, R. et al.*, 2003]. In addition to colony size,
515 *Microcystis* buoyancy is a function of *Microcystis* strain and light exposure history, as it affects
516 gas vacuole and carbohydrate content of the cells [*Ibelings, B. W. et al.*, 1991; *Xiao, Y. et al.*,
517 2012]. Further research is necessary to define buoyant velocities over a wide size range of Lake
518 Erie *Microcystis* under a variety of environmental conditions. Our results, while limited in size
519 range, do show similarity between the > 200 μm values of Nakamura et al. [1993] and samples
520 from two different dates in Lake Erie, and support using the lower estimate of buoyancy (Fig. 4b,
521 N93 3 Aug.) from Nakamura et al. [1993].

522 For the model simulations, we assigned buoyant velocities to Lagrangian particles by random
523 sampling with replacement from the frequency distributions shown in Figure 4c, which were
524 obtained by applying the regression lines (Fig. 4b) from the data of Nakamura et al. [1993] to the
525 diameter frequency distribution from the 8 August 2014 sample from Lake Erie (Fig. 4a). We
526 tested the sensitivity of 1D model simulations to the two buoyant velocity frequency distributions
527 shown in Figure 2c, and refer to these hereafter as "N93 3 Aug" and "N93 18 Sep". Example
528 time series of concentration profiles simulated with the low estimate of buoyancy (N93 3 Aug)
529 are shown in Figure 2e.

530 ### 3.3 Vertical profiles of cyanobacterial concentration and temperature

531 We tested the ability of the random-walk model with buoyancy to simulate realistic *Microcystis*
532 concentration profiles by comparing measured profiles of cyanobacterial chlorophyll

533 concentration from Lake Erie (predominantly *Microcystis*) to corresponding 1D simulations. On
534 20 July, the concentration profile showed strong accumulation within the surface two meters
535 (Fig. 5a), which corresponded to a surface mixed layer defined by a thermocline at 2-m depth
536 (Fig. 5b). A second profile was measured on 9 September, which showed concentration
537 enrichment within a 3-m thick surface mixed layer (Fig. 5c), which was similarly defined by a
538 thermocline at 3-m depth (Fig. 5d).

539 The temperature difference across the thermocline in both cases was only about 1 °C (Fig. 5b,d),
540 but the FVCOM simulations indicated that such subtle stratification features can have a strong
541 influence on diffusivity (e.g., Fig. 2a,b). The accuracy of temperature simulations in
542 hydrodynamic models is often only within a few degrees, which brings into question whether the
543 subtle stratification features that are influencing the *Microcystis* vertical distribution can be
544 reasonably simulated by a hydrodynamic model. Even though the simulated temperature profiles
545 have a warm bias of 1-2 °C, at these locations and times, they show thermoclines at multiple
546 levels that are similar to the observed profiles (Fig. 5b,d). The deeper thermocline may have
547 formed due to convective deepening of the SML overnight, followed by surface warming during
548 the day that produced the shallower thermocline; the profiles were captured in the afternoon. It is
549 the static stability of the profile rather than the absolute temperature that is important in
550 simulation of the diffusivity, and the static stability of the simulated and observed profiles is in
551 reasonable agreement (Fig. 5b,d). Over the full set of 69 profiles, the frequency distribution of
552 static stability simulated by FVCOM was in reasonable agreement with the observed frequency

553 distribution, although the model was biased slightly less stable than the observations (Fig. 6b,
554 Table 2).

555 Simulated normalized concentration profiles of buoyant particles showed enrichment within the
556 surface mixed layer, similar to the observed profiles (Fig. 5a,c). We calculated the center of mass,
557 σ_m, of the concentration profile as a column-integrated indicator of the vertical distribution of
558 concentration (horizontal lines in Fig. 5a,c). Concentration was weighted toward the surface (σ_m
559 > -0.5) in > 80 % of the observed profiles (Fig. 6a), which is consistent with the assumption to
560 treat *Microcystis* colonies as buoyant particles in the model.

561 We selected the lower estimate of buoyancy (N93 3 Aug) for use in the hindcast simulations. The
562 simulated frequency distribution of σ_m was in reasonable agreement with the observed
563 distribution for both the low and high estimates of w_b, although the low estimate was closer to the
564 observations (Fig. 6a, Table 2). Similarly, the direct measurements of w_b also indicated better
565 agreement with the lower estimate of buoyancy (Fig. 4b).

566 ### 3.4 Hindcast simulations of CHAB intensity and distribution

567 Having shown that 1D random walk simulations reasonably approximated the changing vertical
568 distributions of buoyant *Microcystis* colonies in response to varying turbulence, we went on to
569 test whether inclusion of this mechanism in the forecast model improved model skill. Hindcast
570 simulations were initiated from each of the 26 quality satellite images of CHAB distribution for
571 the 2011 CHAB season.

572 In one example, a hindcast simulation was initialized on 6 August, which was a calm day (wind <
573 5 m s^{-1}) with an intense CHAB event throughout the central western basin (Fig. 7a). On the
574 following day, wind increased (5-10 m s^{-1}), and a second satellite image indicated reduced
575 surface CHAB intensity and distribution (Fig. 7d). The 3D simulation captured the reduced
576 surface CHAB intensity on 7 August, while the 2D model did not, which can be seen
577 qualitatively by comparing Figures 7e and 7f, and was indicated quantitatively by reduced
578 frequency bias (B) of the 3D simulation compared to the 2D simulation (3D B = 1.10; 2D B =
579 1.34). On day 9 (15 Aug.), the simulated CHAB distribution was distinctly different between the
580 2D and 3D models (Fig. 7h,i). In comparison to the 2D model, the 3D model CHAB distribution
581 was more similar to the observed distribution (3D PSS = 0.56; 2D PSS = 0.41), having less
582 CHAB coverage in the central basin east of Sandusky and more continuous coverage along the
583 coast from Monroe to Toledo. Both 2D and 3D models simulated the advection of CHAB to Port
584 Clinton (Fig 7b,c and h,i), which was minimally affected by CHAB on 6 August and fully
585 covered on 15 August (Fig. 7a,g).

586 In a second example, a hindcast simulation was initialized on 29 August, which was a date with
587 only partial coverage by the satellite image, leaving no data over much of the western basin (Fig.
588 8a). Output from a previous model run was used to initialize the CHAB distribution in the
589 western basin (Fig. 8b,c). On simulation day four (2 Sept.) a second partial satellite image
590 indicated extensive CHAB coverage in the western basin (Fig. 8d), consistent with both models.
591 Both 2D and 3D models underestimated the CHAB coverage, although the 3D model better
592 matched the observed coverage (2D B = 0.81, PSS = 0.76; 3D B = 0.90, PSS = 0.84; Fig. 8d,e,f).

593 The partial image on 2 September did not show the extensive CHAB outbreak into the central
594 basin east of Leamington, Ontario, although it was simulated by both 2D and 3D models (Fig.
595 8e,f), and was revealed the following day in the 3 September satellite image (Fig. 8g). The 3D
596 model better simulated the CHAB distribution on simulation day 5 (3 Sept.) than the 2D model
597 (2D B = 0.79, PSS = 0.68; 3D B = 0.99, PSS = 0.80; Fig. 8g,h,i).

598 The examples in Figures 7 and 8 show, that both 2D and 3D models capture some observed
599 events that may be attributed to advection, but the 3D model performed better in several cases.
600 The 3D model is initialized with a better estimate of total biomass than the 2D model because an
601 estimate of the surface mixed layer depth for buoyant *Microcystis* colonies is used to assign the
602 depth over which the satellite-derived surface concentration is applied. In addition, the 3D model
603 is able to simulate changing surface concentration in response to changing mixed layer depth.
604 Finally, the 3D model produced different final CHAB spatial distribution than the 2D model,
605 which likely results from the more accurate vertical distribution within a complex 3D flow field.

606 ### 3.5 Summary of hindcast skill statistics

607 Skill statistics were summarized by simulation day to evaluate how long the model can be run
608 from initialization before skill begins to decline. The Pierce skill score (PSS) gave positive values
609 for the 2D model, 3D model, and the persistence forecast on simulation days 1-10 (Fig. 9).
610 Positive values of PSS indicate that the hit rate was greater than the false positive rate, and
611 therefore the model had greater skill than a random forecast or constant CHAB or no-CHAB
612 prediction [*Hogan, R. J. and I. B. Mason*, 2012]. The frequency bias was less than 1.0 on 8 of 10
613 forecast days, indicating that both models had an overall bias toward under-prediction, although

614 not consistently so (Fig. 9a,b). The 95% confidence intervals on the difference in PSS indicated
615 that the 3D model displayed significantly greater skill in the hindcast simulations than the
616 persistence forecast through simulation day 6, and was not significantly worse than the
617 persistence forecast through day 10 (Fig. 10). The 3D model had significantly greater skill than
618 the 2D model over the full simulation period. The 2D model had significantly less skill than the
619 persistence forecast on all simulation days (Fig. 10).

620 It may be surprising that the persistence forecast displayed a reasonable level of skill. This can be
621 explained in that the spatial distribution of CHABs in Lake Erie has a number of persistent
622 features. For example CHABs often persist in the southern and western portions of the western
623 basin, while they are rarely present in the Detroit River plume and in the central basin east of the
624 islands, as indicated by 13 years of Lake Erie CHAB spatial patterns compiled by Wynne and
625 Stumpf [2015]. The model does not necessarily preserve these persistent features. For example
626 CHABs may be erroneously flushed from Maumee Bay in long simulations, although this
627 happened to a lesser extent in the 3D model than in the 2D model (Fig. 7g,h,i). The skill of the
628 persistence forecast indicates that the most recent satellite image is a reasonable indication of the
629 CHAB distribution for several days after.

630 Skill statistics based on pixel-by-pixel comparisons, and use of a persistence forecast as a
631 benchmark, provide a useful point of comparison among models, but do not capture all aspects of
632 model performance. For example, the large simulated plume that extended into the central basin
633 on 3 September (Fig. 8g,h,i) does not exactly match the observed plume in terms of shape and
634 position. This pattern mismatch detracted from pixel-by-pixel skill statistics, but both models

635 provided information regarding the existence of this transport event before it could be seen in
636 satellite imagery; information that would be useful to forecast users even if the shape of the
637 plume is not entirely accurate. A persistence forecast can score reasonably well in skill statistics
638 that compare spatial patterns, but cannot provide any information on likely transport trajectories.
639 Therefore, even though the 2D model had less skill than the persistence forecast (Fig. 10), this
640 does not indicate that the 2D model has no value because it may provide useful information on
641 likely transport trajectories. It is a challenge to formulate skill statistics that test for accuracy in
642 simulation of transport events, largely because it is difficult to identify and quantify transport
643 events by comparing among subsequent satellite images. Wynne et al. [2011] attempted to
644 calculate skill statistics based on movement of the bloom centroid; however, this approach is
645 likely to work only for special cases because accurate calculation of the bloom centroid is
646 sensitive to missing data (cloud cover) and the bloom often consists of multiple patches that may
647 move in different directions rather than one distinct patch. Formulation of appropriate skill
648 statistics for CHAB forecasts is an area for further work.

649 ### 3.6 Ecological significance

650 Aside from the specific application of CHAB forecasting, the observations and simulations
651 shown here provide interesting insights on the physical processes that influence phytoplankton
652 ecology in a polymictic lake. Previous studies of Lake Erie circulation and thermal structure
653 considered the western basin to be largely unstratified [e.g., *Beletsky, D. et al.*, 2013], but our
654 study highlighted the importance of fine-scale thermal structure in the western basin in a
655 biological context. Surface mixed layer depth varies hour by hour due to subtle features in the

temperature profile caused by the diel cycle of surface heating and cooling, further modified by varying wind stress. Colony buoyancy is sufficient to keep *Microcystis* concentrated within the constantly changing surface mixed layer depth. The thermal structure is subtle in comparison to the continuous seasonal stratification that occurs in deeper lakes, and in the central and eastern basins of Lake Erie, but important nonetheless to the *Microcystis* vertical distribution. The position of *Microcystis* colonies in the water column is critical to their light exposure, nutrient acquisition, and ultimately to their ability to dominate the phytoplankton community, and produce toxic blooms.

4 Acknowledgements

M. D. Rowe received funding from the Great Lakes Restoration Initiative through the US Environmental Protection Agency and National Oceanic and Atmospheric Administration. The FVCOM model and Lagrangian particle tracking model code are available from http://fvcom.smast.umassd.edu/. David Schwab, University of Michigan, modified the Lagrangian code for improved efficiency. Duane Gossiaux, NOAA GLERL, measured colony size distributions by microscopy. Danna Palladino and Ashley Burtner, CILER, collected field samples from Lake Erie in 2012, 2013 and 2014. We are grateful to Ulf Gräwe, Leibniz Institute for Baltic Sea Research, for providing code for alternative random walk numerical schemes. Data and model results are available upon request from the corresponding author (mark.rowe@noaa.gov). This is GLERL Contribution No. XXXX.

5 References

Anderson, E. J., A. J. Bechle, C. H. Wu, D. J. Schwab, G. E. Mann, and K. A. Lombardy (2015), Reconstruction of a meteotsunami in Lake Erie on 27 May 2012: Roles of atmospheric conditions on hydrodynamic response in enclosed basins, *J. Geophys. Res.: Oceans*, *120*, 8020-8038, doi:10.1002/2015JC010883.

Anderson, E. J., and M. S. Phanikumar (2011), Surface storage dynamics in large rivers: Comparing three‐dimensional particle transport, one‐dimensional fractional derivative, and multirate transient storage models, *Water Resour. Res.*, *47*(9), W09511.

Anderson, E. J., and D. J. Schwab (2013), Predicting the oscillating bi-directional exchange flow in the Straits of Mackinac, *J. Great Lakes Res.*, *39*(4), 663-671.

Anderson, E. J., D. J. Schwab, and G. A. Lang (2010), Real-Time Hydraulic and Hydrodynamic Model of the St. Clair River, Lake St. Clair, Detroit River System, *J. Hydraul. Eng.*, *136*, 507.

Bai, X., J. Wang, D. J. Schwab, Y. Yang, L. Luo, G. A. Leshkevich, and S. Liu (2013), Modeling 1993–2008 climatology of seasonal general circulation and thermal structure in the Great Lakes using FVCOM, *Ocean Model.*, *65*, 40-63.

Beletsky, D., N. Hawley, and Y. R. Rao (2013), Modeling summer circulation and thermal structure of Lake Erie, *J. Geophys. Res.: Oceans*, *118*(11), 6238-6252.

Bridgeman, T. B., J. D. Chaffin, and J. E. Filbrun (2013), A novel method for tracking western Lake Erie Microcystis blooms, 2002–2011, *J Great Lakes Res*, *39*(1), 83-89.

Brittain, S. M., J. Wang, L. Babcock-Jackson, W. W. Carmichael, K. L. Rinehart, and D. A. Culver (2000), Isolation and characterization of microcystins, cyclic heptapeptide hepatotoxins from a Lake Erie strain of *Microcystis aeruginosa*, *J. Great Lakes Res.*, *26*(3), 241-249.

Bundy, M. H., T. F. Gross, H. A. Vanderploeg, and J. R. Strickler (1998), Perception of inert particles by calanoid copepods: behavioral observations and a numerical model, *J. Plankton Res.*, *20*(11), 2129-2152.

Catherine, A., N. Escoffier, A. Belhocine, A. Nasri, S. Hamlaoui, C. Yéprémian, C. Bernard, and M. Troussellier (2012), On the use of the FluoroProbe®, a phytoplankton quantification method based on fluorescence excitation spectra for large-scale surveys of lakes and reservoirs, *Wat. Res.*, *46*(6), 1771-1784.

Chaffin, J. D., T. B. Bridgeman, S. A. Heckathorn, and S. Mishra (2011), Assessment of *Microcystis* growth rate potential and nutrient status across a trophic gradient in western Lake Erie, *J. Great Lakes Res.*, *37*(1), 92-100.

Chen, C., H. Liu, and R. C. Beardsley (2003), An unstructured grid, finite-volume, three-dimensional, primitive equations ocean model: application to coastal ocean and estuaries, *J. Atmos. Oceanic Technol.*, *20*(1), 159-186.

712 Chorus, I., and J. Bartram (1999), Toxic cyanobacteria in water: a guide to their public health
713 consequences, monitoring and management *Rep.*, 400 pp, World Health Organization, London.

714 Churchill, J. H., J. Runge, and C. Chen (2011), Processes controlling retention of spring‐spawned
715 Atlantic cod (Gadus morhua) in the western Gulf of Maine and their relationship to an index of
716 recruitment success, *Fish. Oceanogr.*, *20*(1), 32-46.

717 French, R., L. Cargnelli, and M. C. Doyle (2011), Lake Erie Binational Nutrient Management
718 Strategy: Protecting Lake Erie by Managing Phosphorus *Rep.*, 30 pp, Lake Erie Lakewide
719 Management Plan Nutrient Management Task Group,
720 http://www.epa.gov/lakeerie/binational_nutrient_management.pdf.

721 Galperin, B., L. Kantha, S. Hassid, and A. Rosati (1988), A quasi-equilibrium turbulent energy
722 model for geophysical flows, *J. Atmos. Sci.*, *45*(1), 55-62.

723 Gilbert, C., W. Gentleman, C. Johnson, C. DiBacco, J. Pringle, and C. Chen (2010), Modelling
724 dispersal of sea scallop (*Placopecten magellanicus*) larvae on Georges Bank: the influence of
725 depth-distribution, planktonic duration and spawning seasonality, *Prog. Oceanogr.*, *87*(1), 37-48.

726 GLWQA Annex 4 (2015), Recommended Phosphorus Loading Targets for Lake Erie, Annex 4
727 Objectives and Targets Task Team Final Report to the Nutrients Annex Subcommittee,
728 http://www.epa.gov/glwqa, 70.

729 Gräwe, U. (2011), Implementation of high-order particle-tracking schemes in a water column
730 model, *Ocean Model.*, *36*(1), 80-89.

731 Gräwe, U., E. Deleersnijder, S. H. A. M. Shah, and A. W. Heemink (2012), Why the Euler
732 scheme in particle tracking is not enough: the shallow-sea pycnocline test case, *Ocean Dynam.*,
733 *62*(4), 501-514.

734 Henry, T. (2014), Toledo seeks return to normalcy after do not drink water advisory lifted, *The*
735 *Toledo Blade*, *5 August*.

736 Hogan, R. J., and I. B. Mason (2012), Deterministic forecasts of binary events, *Forecast*
737 *Verification: A Practitioner's Guide in Atmospheric Science, Second Edition*, 31-59.

738 Huret, M., J. Runge, C. Chen, G. Cowles, Q. Xu, and J. Pringle (2007), Dispersal modeling of
739 fish early life stages: sensitivity with application to Atlantic cod in the western Gulf of Maine,
740 *Marine Ecol.: Prog. Ser.*, *347*, 261-274.

741 Ibelings, B. W., L. R. Mur, and A. E. Walsby (1991), Diurnal changes in buoyancy and vertical
742 distribution in populations of Microcystisin two shallow lakes, *Journal of Plankton Research*,
743 *13*(2), 419-436.

744 Kane, D. D., J. D. Conroy, R. P. Richards, D. B. Baker, and D. A. Culver (2014), Re-
745 eutrophication of Lake Erie: Correlations between tributary nutrient loads and phytoplankton
746 biomass, *J. Great Lakes Res.*, *40*(3), 496-501.

747 Kring, S. A., S. E. Figary, G. L. Boyer, S. B. Watson, and M. R. Twiss (2014), Rapid in situ
748 measures of phytoplankton communities using the bbe FluoroProbe: evaluation of spectral

749 calibration, instrument intercompatibility, and performance range, *Can. J. Fish. Aquat. Sci.*,
750 *71*(7), 1087-1095.

751 Kurmayer, R., G. Christiansen, and I. Chorus (2003), The abundance of microcystin-producing
752 genotypes correlates positively with colony size in Microcystis sp. and determines its microcystin
753 net production in Lake Wannsee, *Applied and Environmental Microbiology*, *69*(2), 787-795.

754 Lin, L., G. Appiah-Sefah, and M. Li (2014), Using a laser particle analyzer to demonstrate
755 relationships between wind strength and *Microcystis* colony size distribution in Lake Taihu,
756 China, *J. Freshwater Ecol.*, *30*(3), 425-433, doi:10.1080/02705060.2014.976666.

757 Medrano, E. A., R. Uittenbogaard, L. D. Pires, B. van de Wiel, and H. Clercx (2013), Coupling
758 hydrodynamics and buoyancy regulation in *Microcystis aeruginosa* for its vertical distribution in
759 lakes, *Ecol. Model.*, *248*, 41-56, doi:10.1016/j.ecolmodel.2012.08.029.

760 Michalak, A. M., E. J. Anderson, D. Beletsky, S. Boland, N. S. Bosch, T. B. Bridgeman, J. D.
761 Chaffin, K. Cho, R. Confesor, and I. Daloğlu (2013), Record-setting algal bloom in Lake Erie
762 caused by agricultural and meteorological trends consistent with expected future conditions,
763 *Proc. Natl. Acad. Sci. U. S. A.*, *110*(16), 6448-6452.

764 Nakamura, T., Y. Adachi, and M. Suzuki (1993), Flotation and sedimentation of a single
765 *Microcystis* floc collected from surface bloom, *Water Res.*, *27*(6), 979-983.

766 O'Neil, J., T. W. Davis, M. A. Burford, and C. Gobler (2012), The rise of harmful cyanobacteria
767 blooms: the potential roles of eutrophication and climate change, *Harmful Algae*, *14*, 313-334,
768 doi:10.1016/j.hal.2011.10.027.

769 Obenour, D. R., A. D. Gronewold, C. A. Stow, and D. Scavia (2014), Using a Bayesian
770 hierarchical model to improve Lake Erie cyanobacteria bloom forecasts, *Water Resour. Res.*, *50*,
771 7847-7860, doi:10.1002/2014WR015616.

772 Rinta-Kanto, J. M., E. A. Konopko, J. M. DeBruyn, R. A. Bourbonniere, G. L. Boyer, and S. W.
773 Wilhelm (2009), Lake Erie *Microcystis*: relationship between microcystin production, dynamics
774 of genotypes and environmental parameters in a large lake, *Harmful Algae*, *8*(5), 665-673.

775 Rose, A. (1948), The sensitivity performance of the human eye on an absolute scale, *J. Opt. Soc.*
776 *Am.*, *38*(2), 196-208, doi:10.1364/JOSA.38.000196.

777 Ross, O. N., and J. Sharples (2004), Recipe for 1‐D Lagrangian particle tracking models in

778 space‐varying diffusivity, *Limnol. Oceanogr.: Methods*, *2*(9), 289-302.

779 Ross, O. N., and J. Sharples (2008), Swimming for survival: a role of phytoplankton motility in a
780 stratified turbulent environment, *J. Marine Syst.*, *70*(3), 248-262.

781 Simpson, J., and D. Bowers (1981), Models of stratification and frontal movement in shelf seas,
782 *Deep-Sea Res.*, *28*(7), 727-738.

783 Smagorinsky, J. (1963), General circulation experiments with the primitive equations: I. the basic
784 experiment, *Mon. Weather Rev.*, *91*(3), 99-164.

785 Strickler, J. R. (1985), Feeding currents in calanoid copepods: Two new hypotheses, in
786 *Physiological Adaptations of Marine Animals*, edited by M. S. Laverack, pp. 459-485, Society
787 for Experimental Biology, UK.

788 Stumpf, R. P., and T. T. Wynne (2015), Experimental Lake Erie Harmful Algal Bloom Bulletin
789 (Bulletin 27), www2.nccos.noaa.gov/coast/lakeerie/bulletin.

790 Stumpf, R. P., T. T. Wynne, D. B. Baker, and G. L. Fahnenstiel (2012), Interannual variability of
791 cyanobacterial blooms in Lake Erie, *PLoS One*, *7*(8), e42444, doi:10.1371/journal.pone.0042444.

792 Tomlinson, M. C., R. P. Stumpf, T. T. Wynne, D. Dupuy, R. Burks, J. Hendrickson, and R. S.
793 Fulton III (2016), Relating chlorophyll from cyanobacteria-dominated inland waters to a MERIS
794 bloom index, *Remote Sensing Letters*, *7*(2), 141-149.

795 Vanderploeg, H. A., J. R. Liebig, W. W. Carmichael, M. A. Agy, T. H. Johengen, G. L.
796 Fahnenstiel, and T. F. Nalepa (2001), Zebra mussel (*Dreissena polymorpha*) selective filtration
797 promoted toxic *Microcystis* blooms in Saginaw Bay (Lake Huron) and Lake Erie, *Can. J. Fish.*
798 *Aquat. Sci.*, *58*(6), 1208-1221.

799 Visser, A. (1997), Using random walk models to simulate the vertical distribution of particles in a
800 turbulent water column, *Mar. Ecol. Prog. Ser.*, *158*, 275-281.

801 Wang, C., X. Wu, C. Tian, Q. Li, Y. Tian, B. Feng, and B. Xiao (2015), A quantitative protocol
802 for rapid analysis of cell density and size distribution of pelagic and benthic *Microcystis* colonies
803 by FlowCAM, *J. Appl. Phycol.*, *27*(2), 711-720.

804 Wiles, P., L. van Duren, C. Häse, J. Larsen, and J. Simpson (2006), Stratification and mixing in
805 the Limfjorden in relation to mussel culture, *J. Marine Syst.*, *60*(1), 129-143.

806 Wynne, T., R. Stumpf, M. Tomlinson, R. Warner, P. Tester, J. Dyble, and G. Fahnenstiel (2008),
807 Relating spectral shape to cyanobacterial blooms in the Laurentian Great Lakes, *Int. J. Remote*
808 *Sens.*, *29*(12), 3665-3672.

809 Wynne, T. T., and R. P. Stumpf (2015), Spatial and Temporal Patterns in the Seasonal
810 Distribution of Toxic Cyanobacteria in Western Lake Erie from 2002–2014, *Toxins*, *7*(5), 1649-
811 1663.

812 Wynne, T. T., R. P. Stumpf, M. C. Tomlinson, and J. Dyble (2010), Characterizing a
813 cyanobacterial bloom in western Lake Erie using satellite imagery and meteorological data,
814 *Limnol. Oceangr.*, *55*(5), 2025-2036.

815 Wynne, T. T., R. P. Stumpf, M. C. Tomlinson, G. L. Fahnenstiel, J. Dyble, D. J. Schwab, and S.
816 J. Joshi (2013), Evolution of a cyanobacterial bloom forecast system in western Lake Erie:
817 Development and initial evaluation, *J. Great Lakes Res.*, *39*, 90-99.

818 Wynne, T. T., R. P. Stumpf, M. C. Tomlinson, D. J. Schwab, G. Y. Watabayashi, and J. D.
819 Christensen (2011), Estimating cyanobacterial bloom transport by coupling remotely sensed
820 imagery and a hydrodynamic model, *Ecol. Appl.*, *21*(7), 2709-2721.

821 Xiao, Y., N. Gan, J. Liu, L. Zheng, and L. Song (2012), Heterogeneity of buoyancy in response
822 to light between two buoyant types of cyanobacterium *Microcystis*, *Hydrobiologia*, *679*(1), 297-
823 311.

824

825 Table 1. Dates of measurements and model simulations.
826

Measurement or simulation	Date
Well-mixed condition simulations	Aug., 2011
Satellite images, 2D, 3D simulations	26 dates, July to Oct., 2011
Colony size distribution (FlowCam)	4 Aug., 2014
Colony size distribution (microscopy)	Weekly sampling July to Sep., 2012 and 2013
Buoyant velocity measurements	15 and 21 July, 2015
Vertical profiles (FluoroProbe)	Weekly sampling July to Sep., 2015

827
828
829

Table 2. Statistics evaluating the skill of the Lagrangian particle model in simulating the vertical distribution of cyanobacterial chlorophyll concentration (center of mass of the normalized concentration profile) and of FVCOM in simulating temperature profiles (potential energy anomaly). The statistics are the mean bias, root mean square deviation (RMSD), and Pearson correlation coefficient (*r*).

	Bias	RMSD	*r*
Center of mass, N93 18 Sep, σ	0.04	0.09	0.56
Center of mass, N93 3 Aug, σ	-0.01	0.08	0.53
Potential energy anomaly, J m^{-3}	-0.20	0.72	0.83

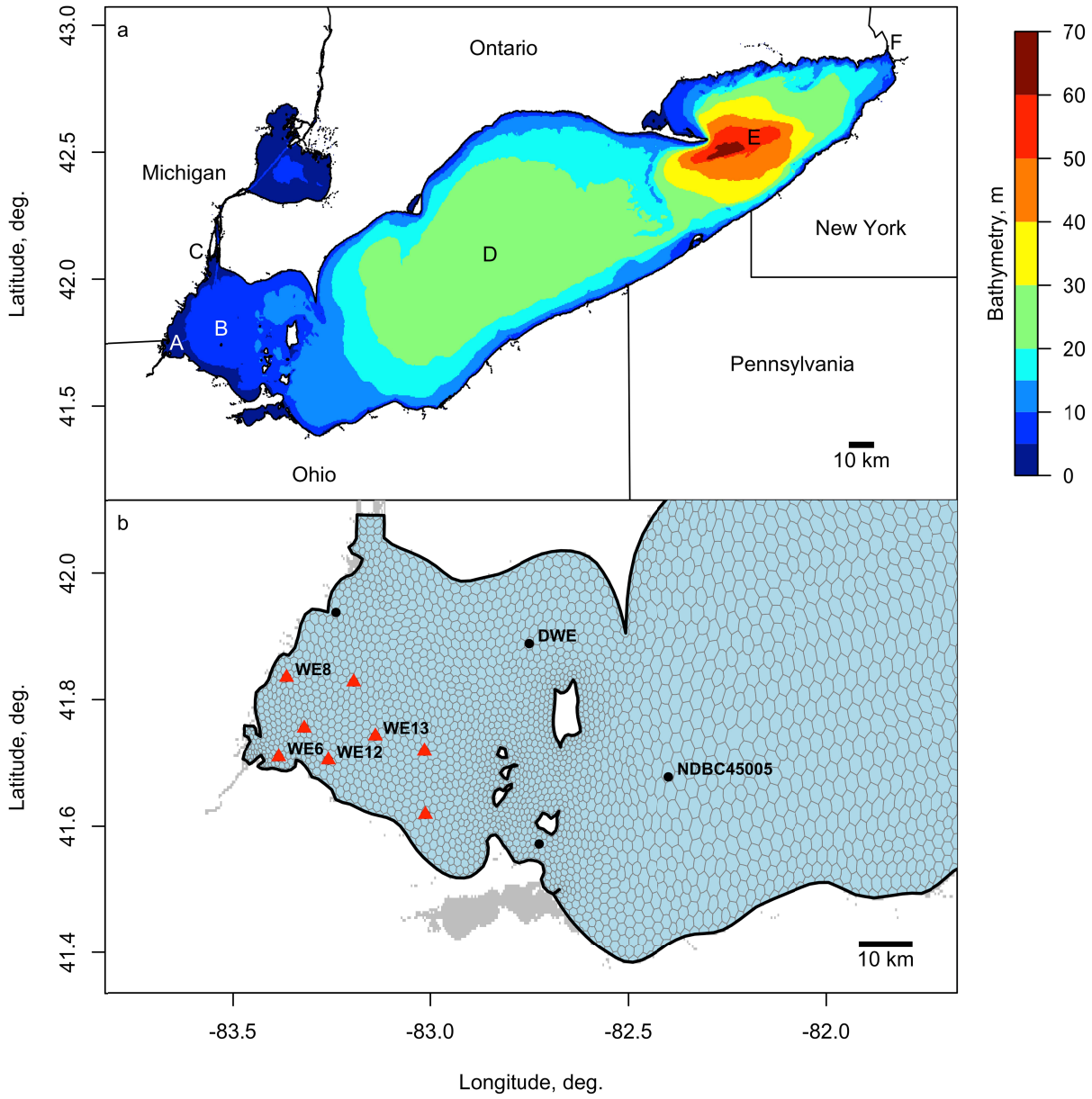

836

837 Figure 1. a) Geographic location and bathymetry of Lake Erie, showing bordering U.S. states and

838 the Canadian province of Ontario. Features of interest are identified, including A) Maumee Bay,

839 B) Western Basin, C) Gibraltar on the Detroit River, D) Central Basin, E) Eastern Basin, and F)

840 Buffalo on the Niagara River. b) An enlarged view of the western portion of the FVCOM model
841 domain. FVCOM domain boundaries are indicated with a heavy black line, and node-centered
842 tracer control elements with gray lines. Surface mixed layer depth was estimated in hindcast
843 simulations at the stations identified with symbols. Well-mixed condition simulations were
844 conducted at the named stations. Profiles of temperature and cyanobacterial chlorophyll
845 concentration were measured at the stations indicated by red triangles.
846

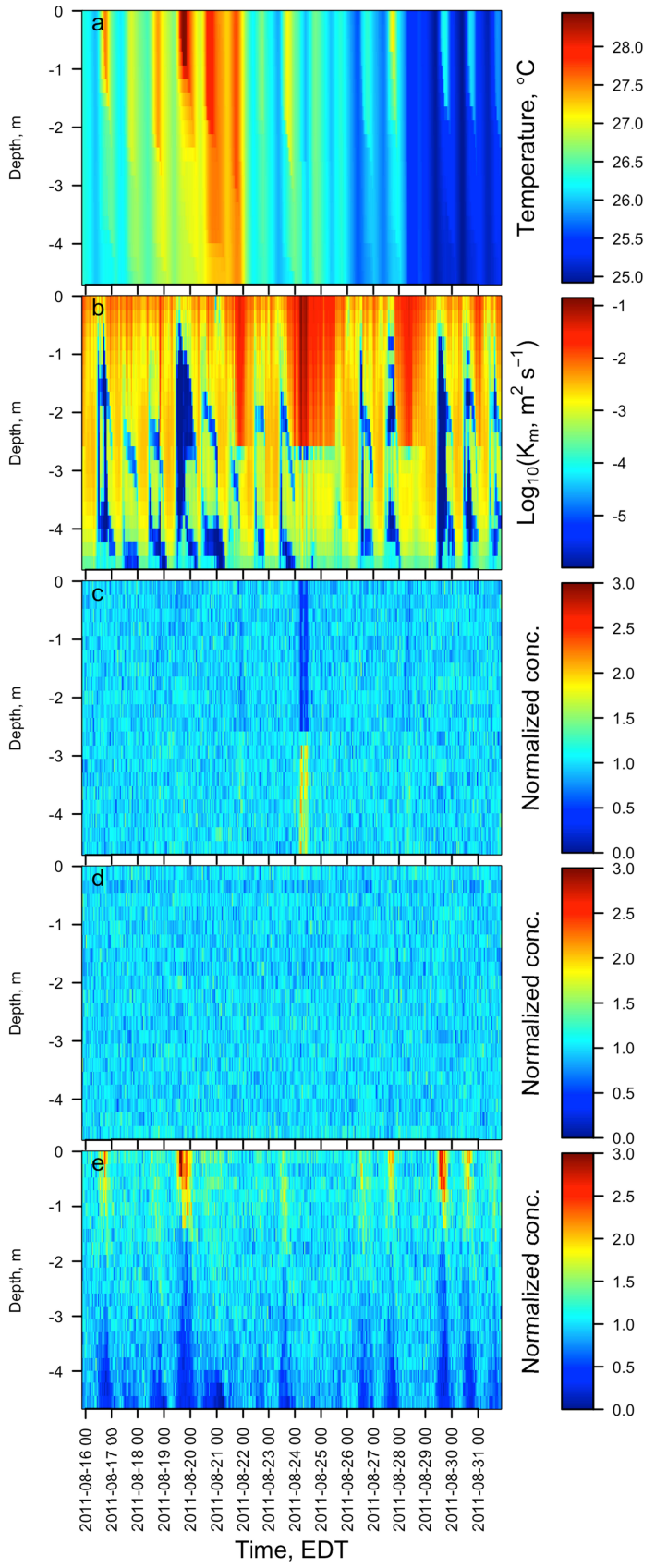

Figure 2. Time series of temperature (a) and diffusivity (b) profiles output from FVCOM for 16-31 August 2011 at station WE8. Time series of normalized concentration profiles from 1-D vertical random walk simulations without buoyancy (well-mixed condition test) using the Visser scheme with fixed 1 s time step (c), and Visser scheme with variable time step (d) set according to the Visser criterion (Eq. 4). A 1-D simulation with buoyancy (N93 3 Aug) using the Visser scheme and variable time step (e). Artificial accumulation of particles in a low diffusivity area with associated depletion in the upper half of the water column can be seen on 24 August (c), with improved performance from the variable time step (d).

847

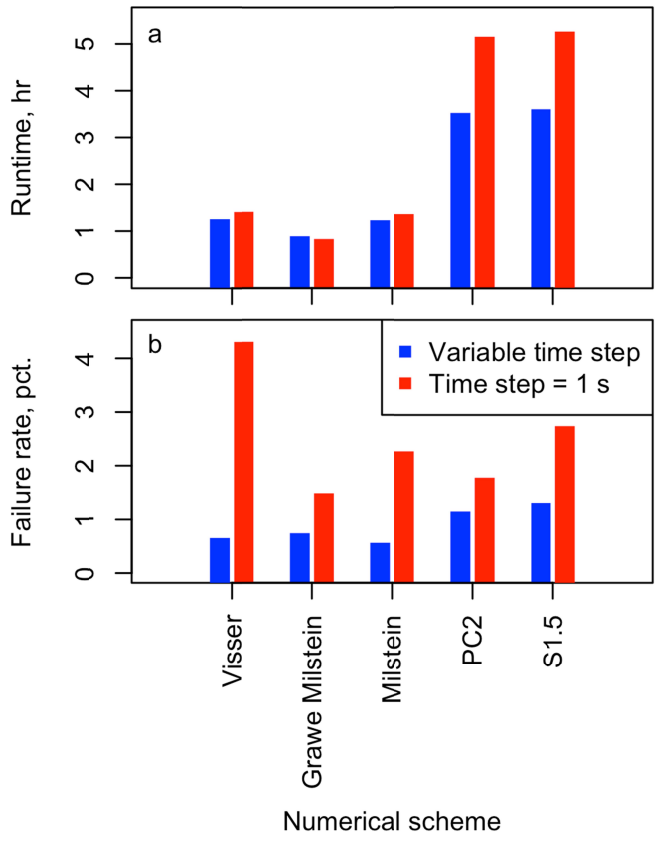

Figure 3. Performance comparison of the five vertical random walk numerical schemes and the variable time step scheme. One-dimensional vertical mixing simulations with 1000 particles were conducted for the month of August, 2011, at the six stations indicated in Figure 1. a) Total run time for the six simulations. b) percent occurrence of failure to meet the quality criterion out of 4464 hourly records. The quality criterion was a signal to noise ratio > 5 where the signal was simulated normalized surface concentration with buoyancy (N93 3 Aug) and the noise was absolute deviation of the normalized surface concentration from 1.0 in a well-mixed condition test (without buoyancy). Concentration was normalized to the mean column concentration.

858

859

860

861

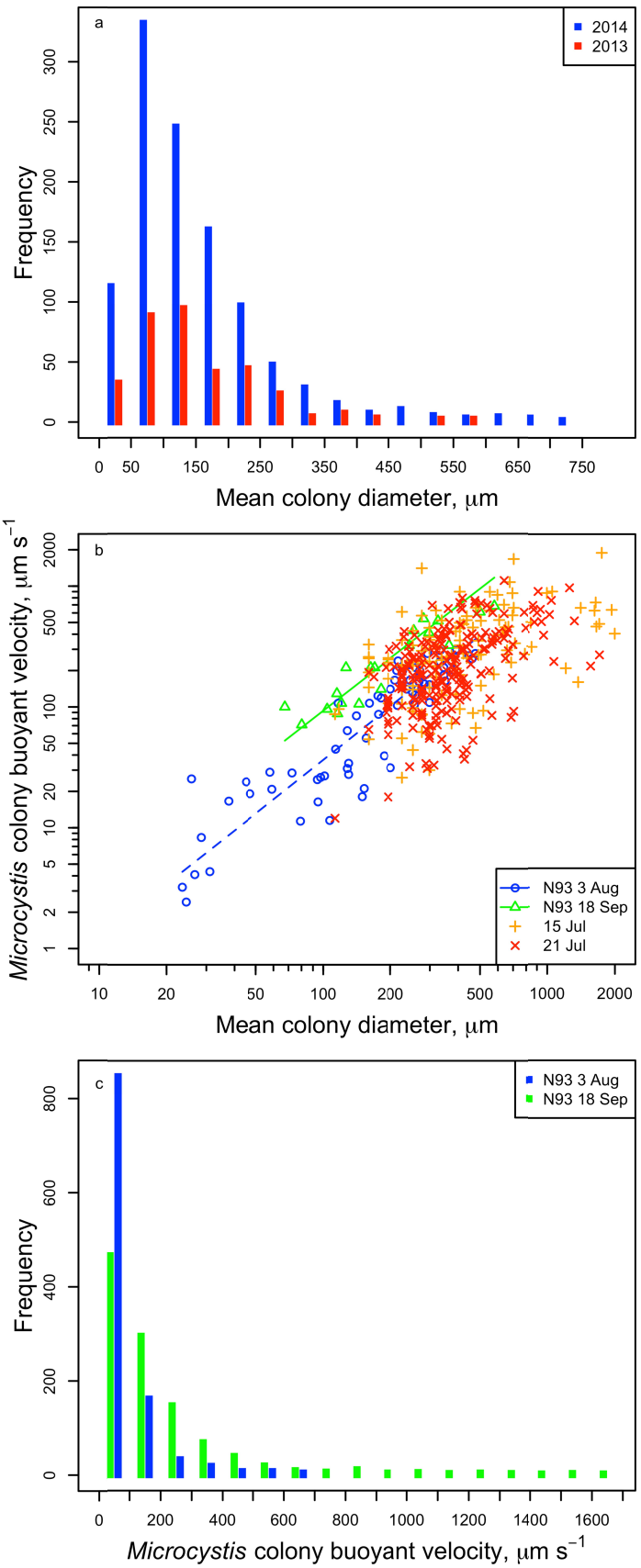

Figure 4. a) Histogram of *Microcystis* colony size distribution for samples collected in Lake Erie in 2013 and 2014. b) *Microcystis* colony buoyant velocity for samples collected in Lake Erie on 15 and 21 July, 2015, and data digitized from Nakamura et al. (1993, their Fig. 3). c) Histogram of *Microcystis* colony buoyant velocity resulting from application of the regression lines in Fig. 2b to the 2015 size distribution in Fig. 2a.

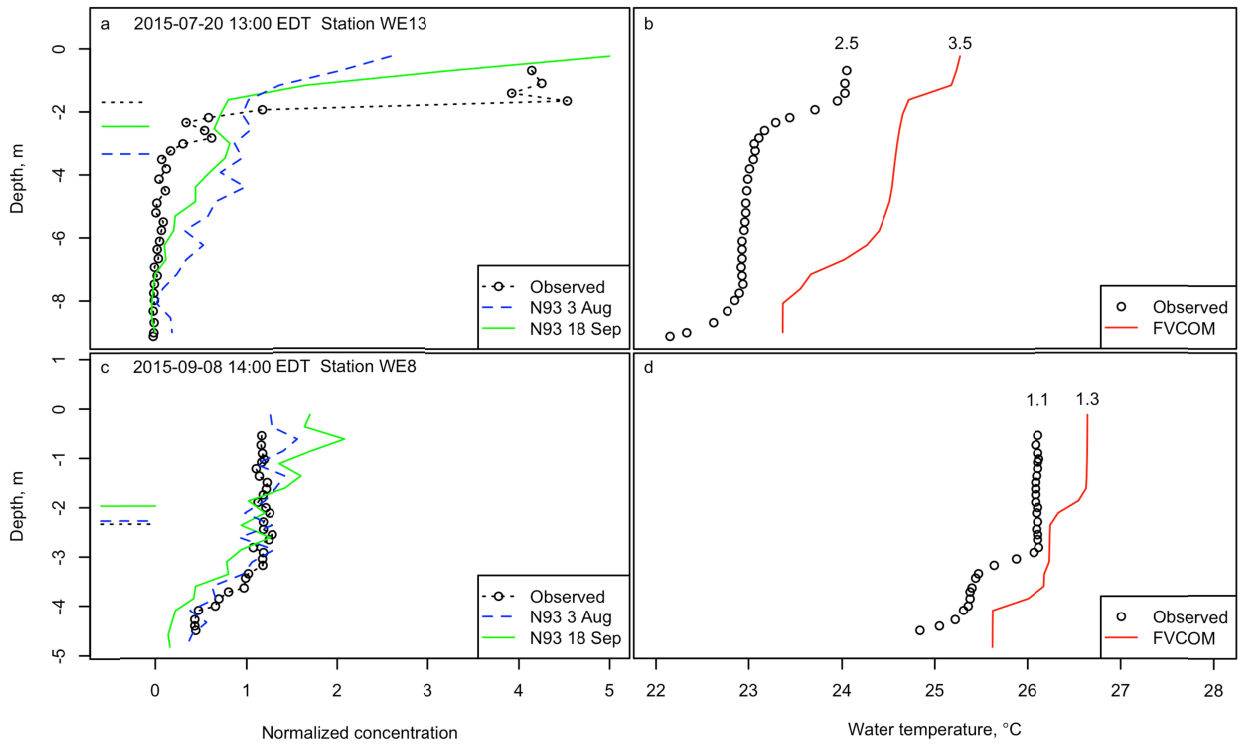

862

863 Figure 5. Two examples of observed vertical profiles of normalized concentration of

864 cyanobacterial chlorophyll and temperature with simulated values plotted for comparison.

865 Horizontal lines indicate the center of mass, σ_m, of the normalized concentration profiles, and the

866 potential energy anomaly, ϕ, J m^{-3}, is given above the temperature profiles.

867

868

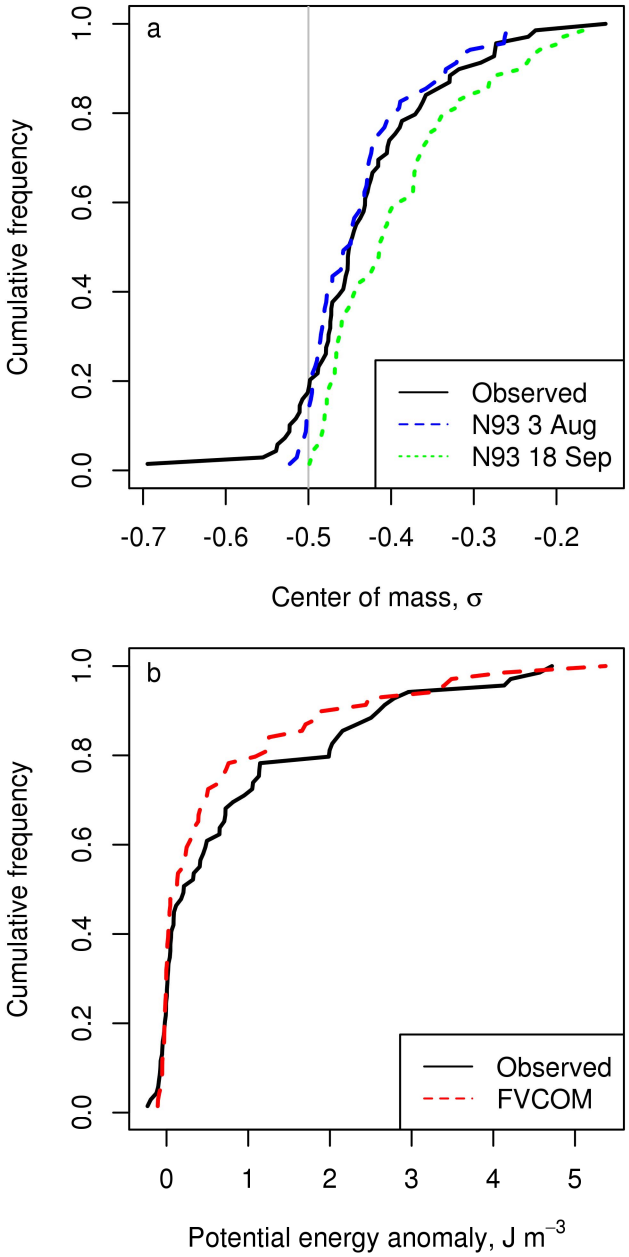

869

870 Figure 6. Cumulative frequency distributions of simulated and observed a) center of mass of the

871 normalized cyanobacteria concentration profile, and b) potential energy anomaly of the

872 temperature profile for 69 profiles collected in July - September of 2015 at stations indicated in

873 Figure 1.

874

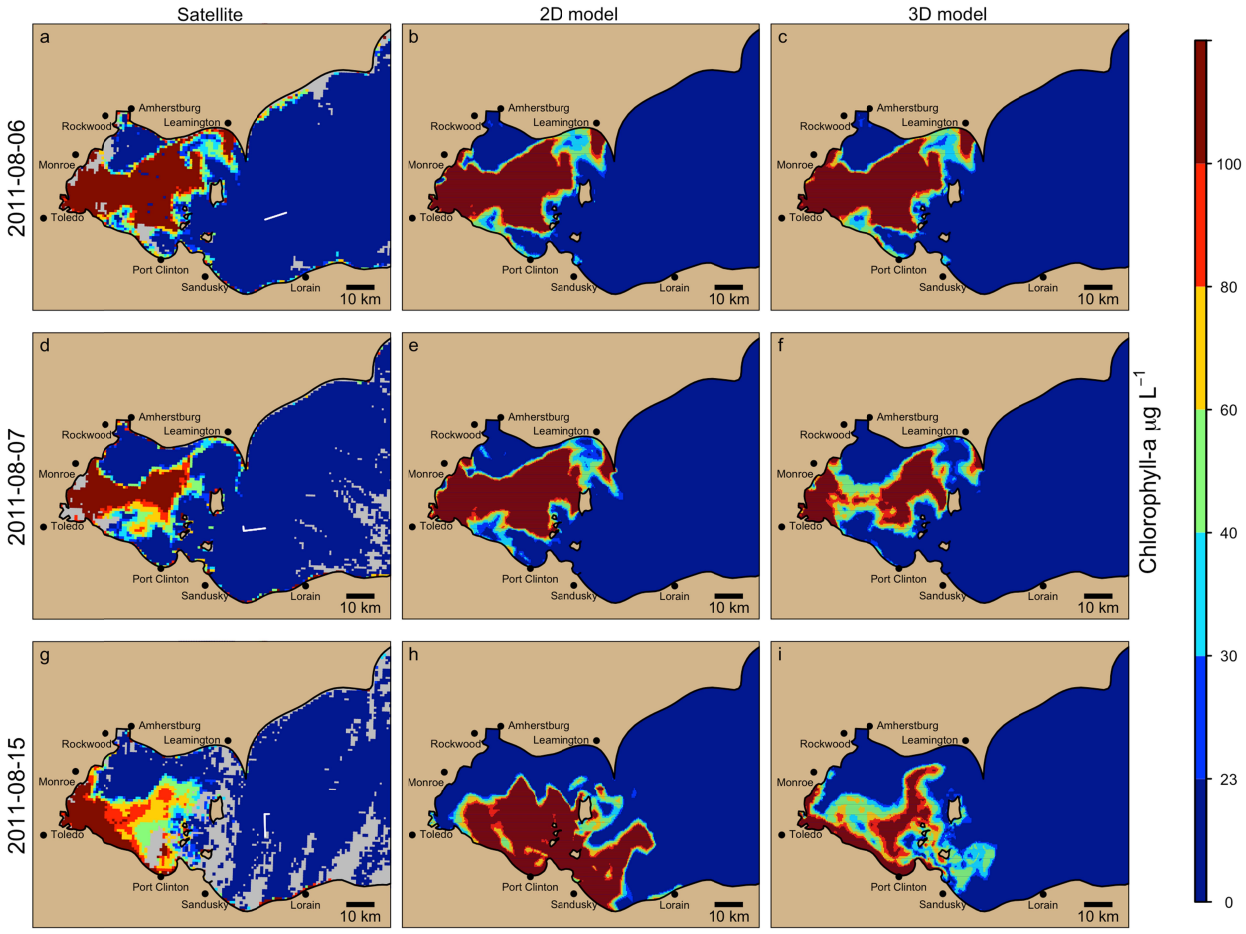

875

876 Figure 7. Comparison of 2D and 3D hindcast simulations initialized from satellite-derived
877 cyanobacterial chlorophyll concentration (a) on 6 August 2011. Subsequent satellite images (d,g)
878 were used for model skill assessment. Gray color indicates missing data. Wind speed, averaged
879 over the preceding 12 hours, was < 5 m s^{-1} on 6 August and increased to 5-10 m s^{-1} on 7 and 15
880 August (wind barbs a,d,g). In the 2D simulation, particles were initiated in the surface 1m and
881 vertical mixing was not simulated (advection only). In the 3D simulation, particles were
882 initialized over the surface mixed layer, as determined by preliminary simulations of 1D mixing
883 with buoyancy, and the model was run with 3D advection in addition to vertical mixing with

884 buoyancy. While both 2D and 3D models simulated CHAB advection toward Port Clinton
885 observed on 15 August, the 3D model better simulated reduced intensity and coverage observed
886 on 7 and 15 August due to higher winds, and continued CHAB coverage near Toledo and
887 Monroe on 15 August.
888

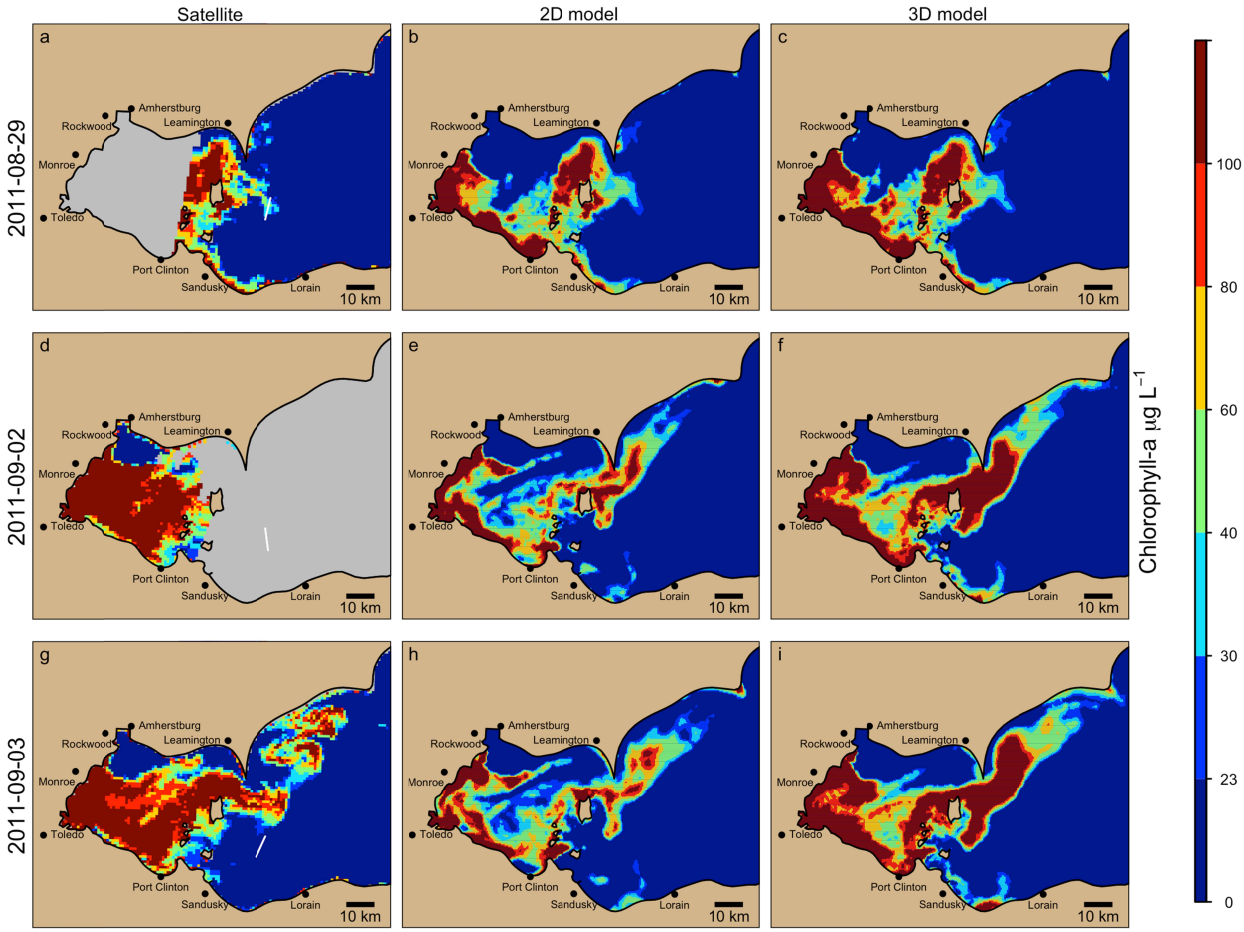

Figure 8. Comparison of 2D and 3D hindcast simulations initialized from satellite-derived cyanobacterial chlorophyll concentration (a) on 29 August 2011. Symbols and model setup are explained in Figure 8. While both 2D and 3D models simulated CHAB advection east of Leamington into the central basin observed on 3 September, the 3D model better simulated CHAB intensity and extent in the western basin observed on 3 September. Wind speed was < 5 m s^{-1} during the simulation period, but was north at 10 m s^{-1} until 12 hours prior to the initial image.

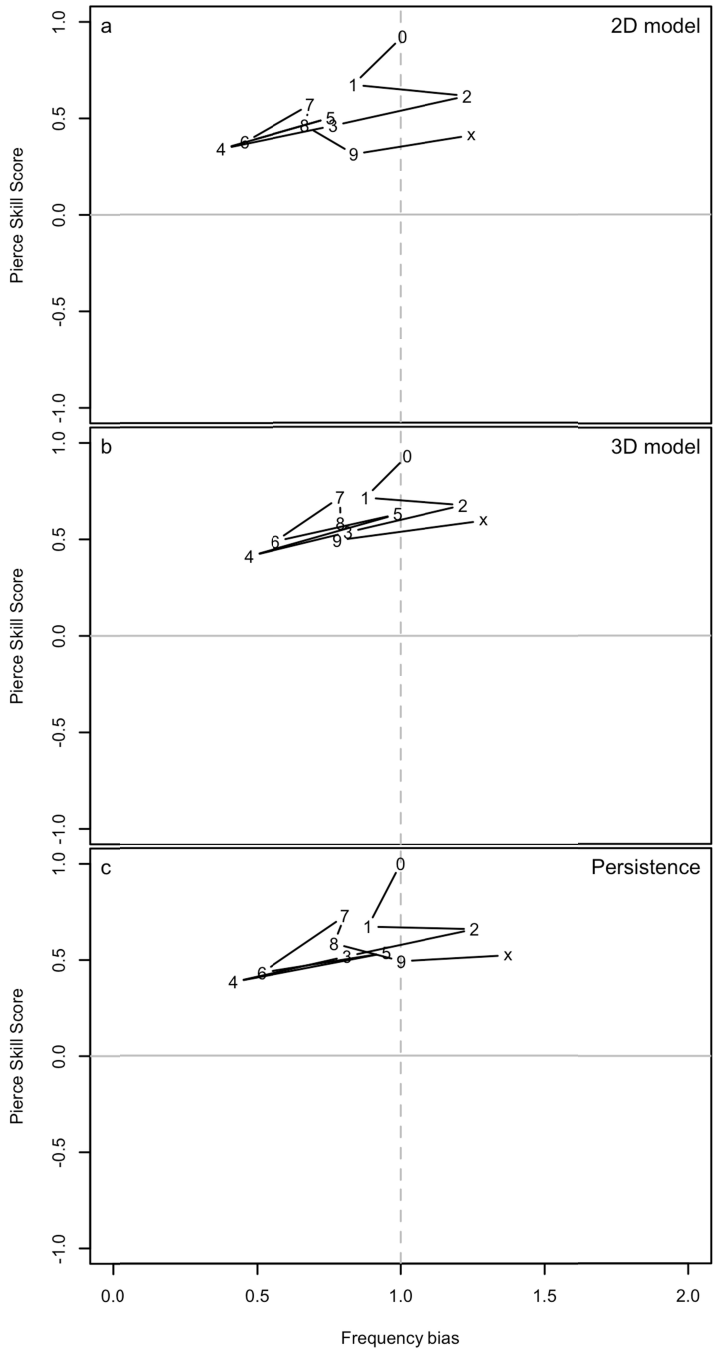

Figure 9. Skill-bias plots for the 2D model (advection only), 3D model (advection, vertical mixing, and buoyancy), and persistence forecasts for the 2011 hindcast simulations. The plot symbol indicates the simulation day (0 = initial, x = day 10). Pierce Skill Score (PSS) is the hit rate minus the false detection rate, and frequency bias (B) is the ratio of forecast hits to observed hits. Positive PSS indicates greater skill than a random forecast. Frequency bias of 1.0 indicates the same number of CHAB pixels were predicted as observed.

897

898

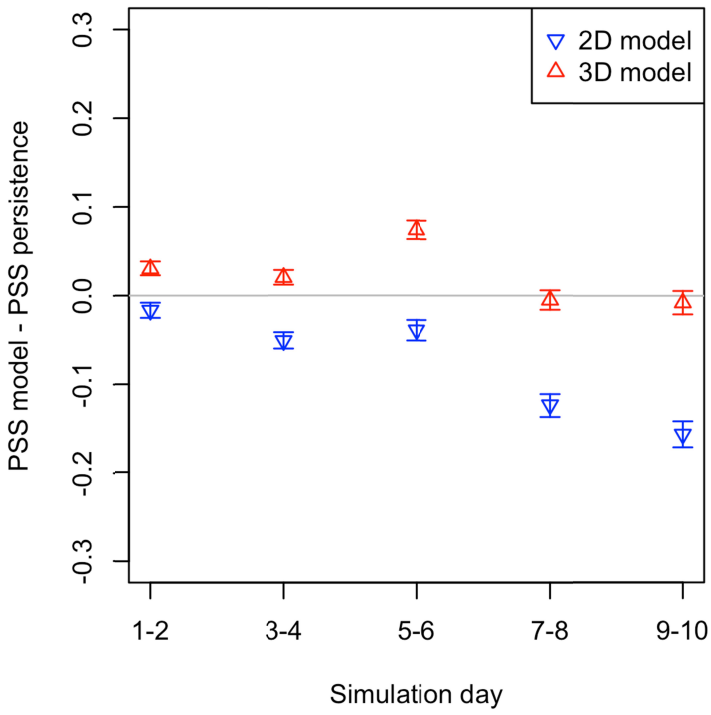

Figure 10. Pierce skill score (PSS) of the model minus PSS of the persistence forecast. Positive values indicate greater skill for the model than for the persistence forecast. Error bars indicate the 95% bootstrap confidence interval on the difference in PSS for the 26 hindcast simulations from the 2011 CHAB season, grouped into two-day intervals. The 3D model (including vertical mixing with buoyancy) had greater skill than the 2D model (advection only) and greater skill than the persistence forecast through day 6 and comparable skill out to day 10.

Figure 1. Figure

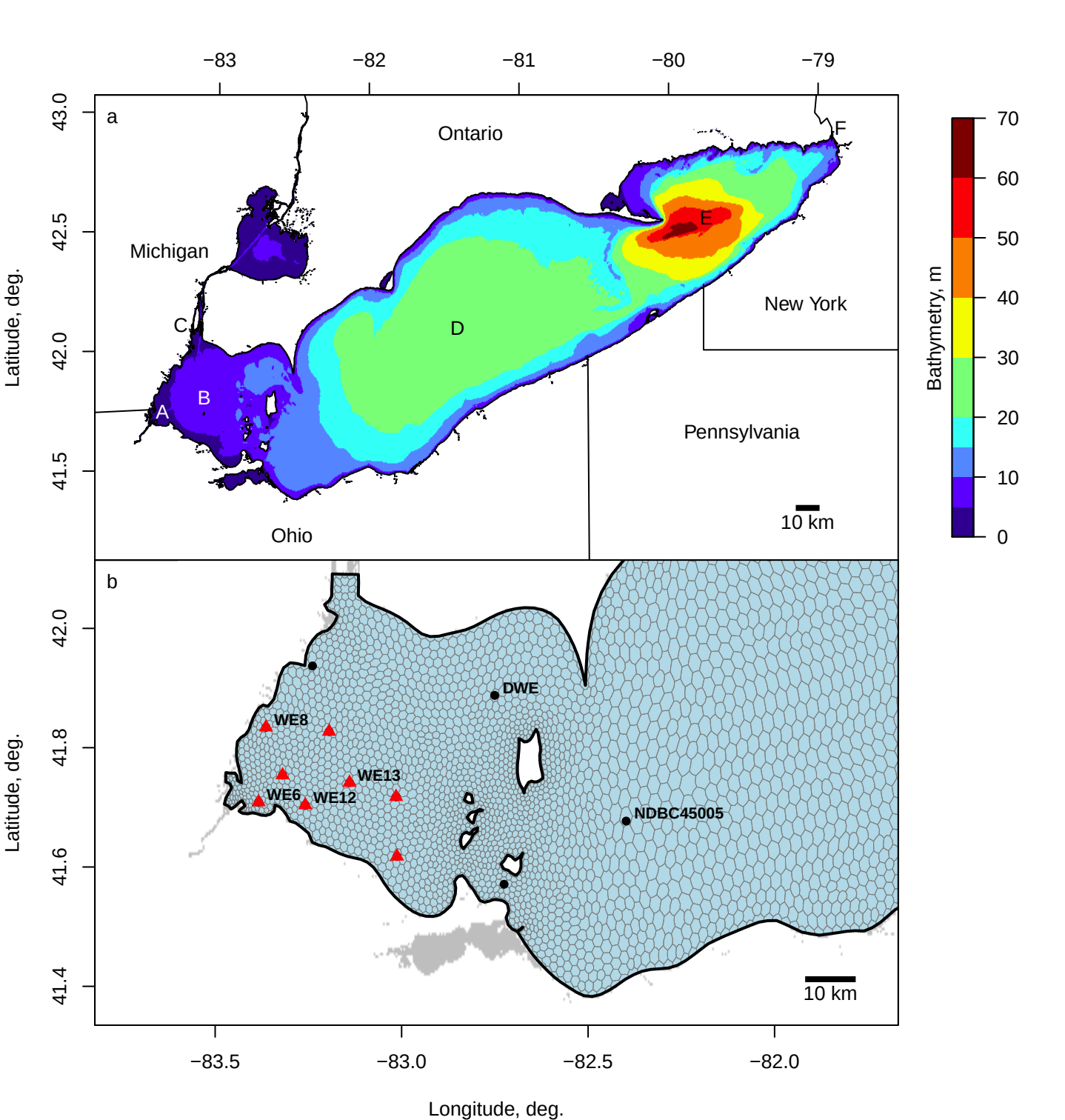
a
Ontario
Michigan
New York
Pennsylvania
Ohio
A
B
C
D
E
F
10 km
Bathymetry, m
70
60
50
40
30
20
10
0
b
DWE
WE8
WE13
WE6
WE12
NDBC45005
10 km
−83
−82
−81
−80
−79
43.0
42.5
42.0
41.5
−83.5
−83.0
−82.5
−82.0
41.8
41.6
41.4
Latitude, deg.
Longitude, deg.

Figure 2. Figure

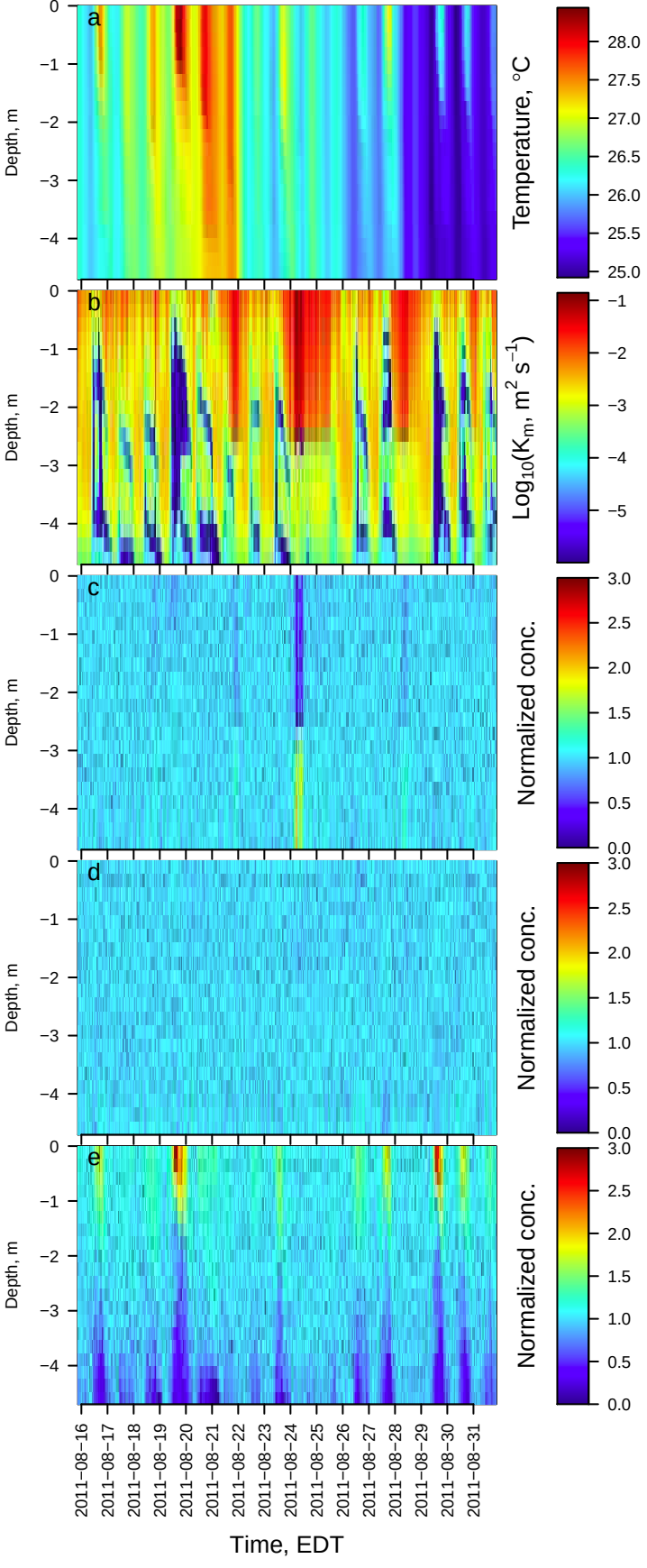
a
b
c
d
e
Depth, m
0
−1
−2
−3
−4
Temperature, °C
28.0
27.5
27.0
26.5
26.0
25.5
25.0
Log10(Km, m2 s−1)
−1
−2
−3
−4
−5
Normalized conc.
3.0
2.5
2.0
1.5
1.0
0.5
0.0
2011−08−16
2011−08−17
2011−08−18
2011−08−19
2011−08−20
2011−08−21
2011−08−22
2011−08−23
2011−08−24
2011−08−25
2011−08−26
2011−08−27
2011−08−28
2011−08−29
2011−08−30
2011−08−31
Time, EDT

Figure 3. Figure

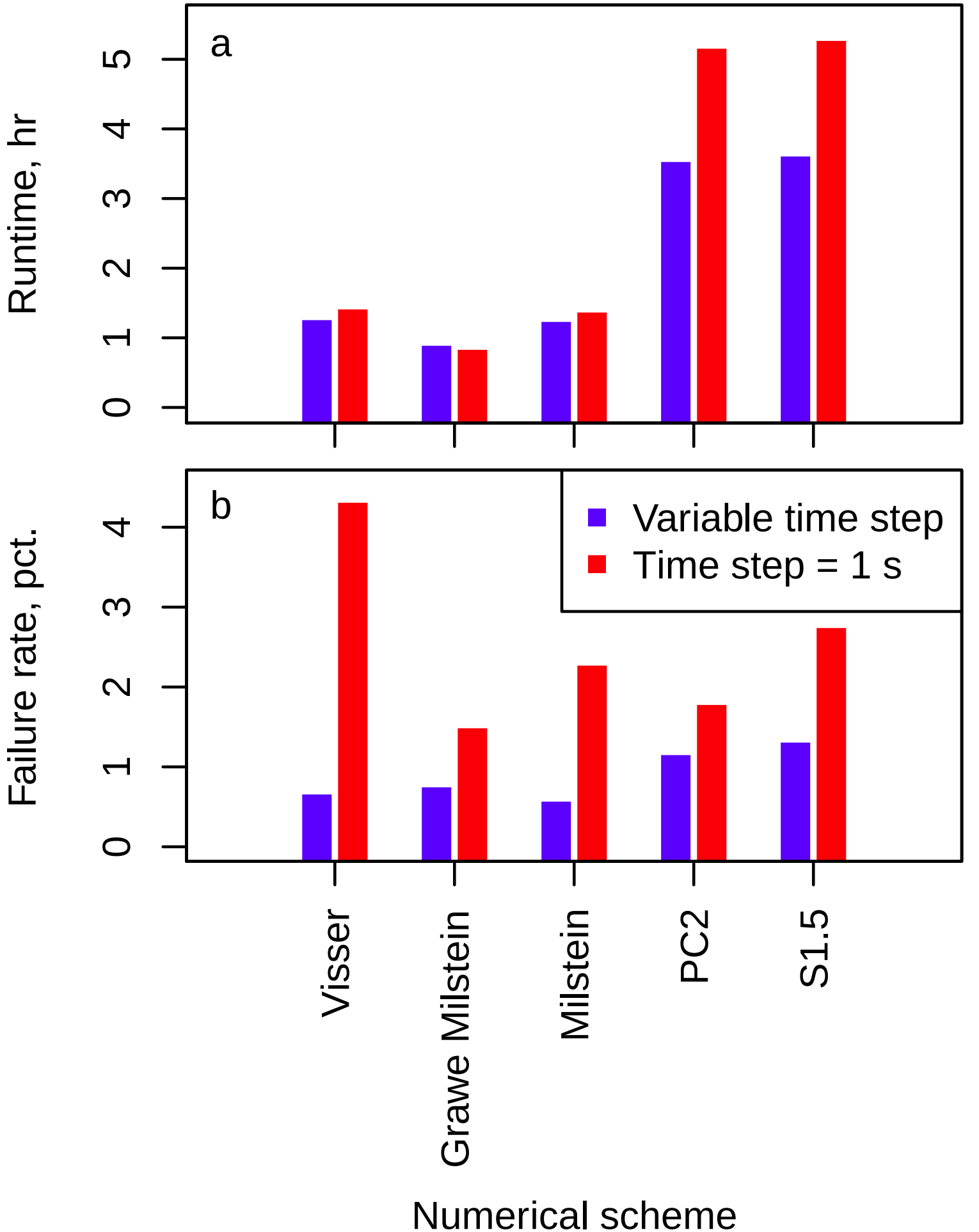
a
Runtime, hr
0
1
2
3
4
5
b
Failure rate, pct.
0
1
2
3
4
Variable time step
Time step = 1 s
Visser
Grawe Milstein
Milstein
PC2
S1.5
Numerical scheme

Figure 4. Figure

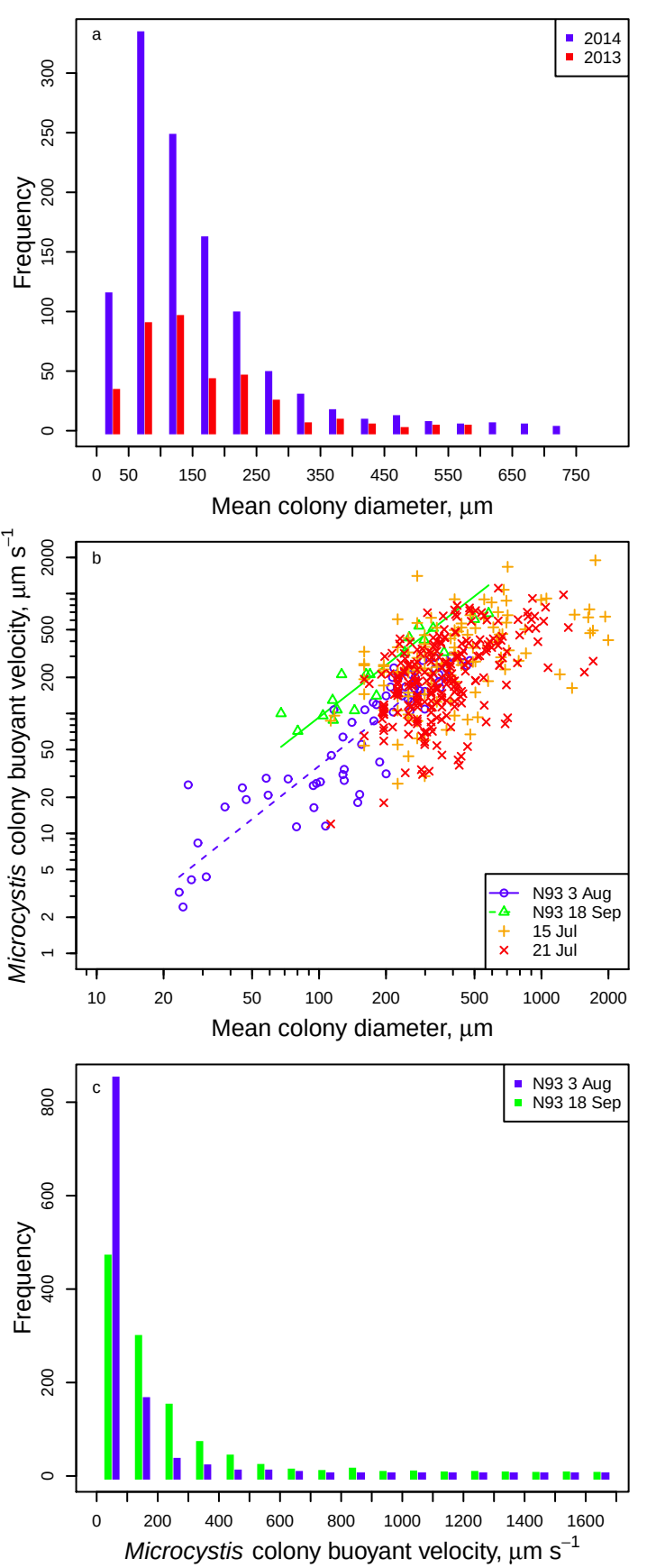
a
2014
2013
Frequency
0
50
100
150
200
250
300
0
50
150
250
350
450
550
650
750
Mean colony diameter, µm
b
Microcystis colony buoyant velocity, µm s−1
1
2
5
10
20
50
200
500
2000
10
20
50
100
200
500
1000
2000
Mean colony diameter, µm
N93 3 Aug
N93 18 Sep
15 Jul
21 Jul
c
N93 3 Aug
N93 18 Sep
Frequency
0
200
400
600
800
0
200
400
600
800
1000
1200
1400
1600
Microcystis colony buoyant velocity, µm s−1

Figure 5. Figure

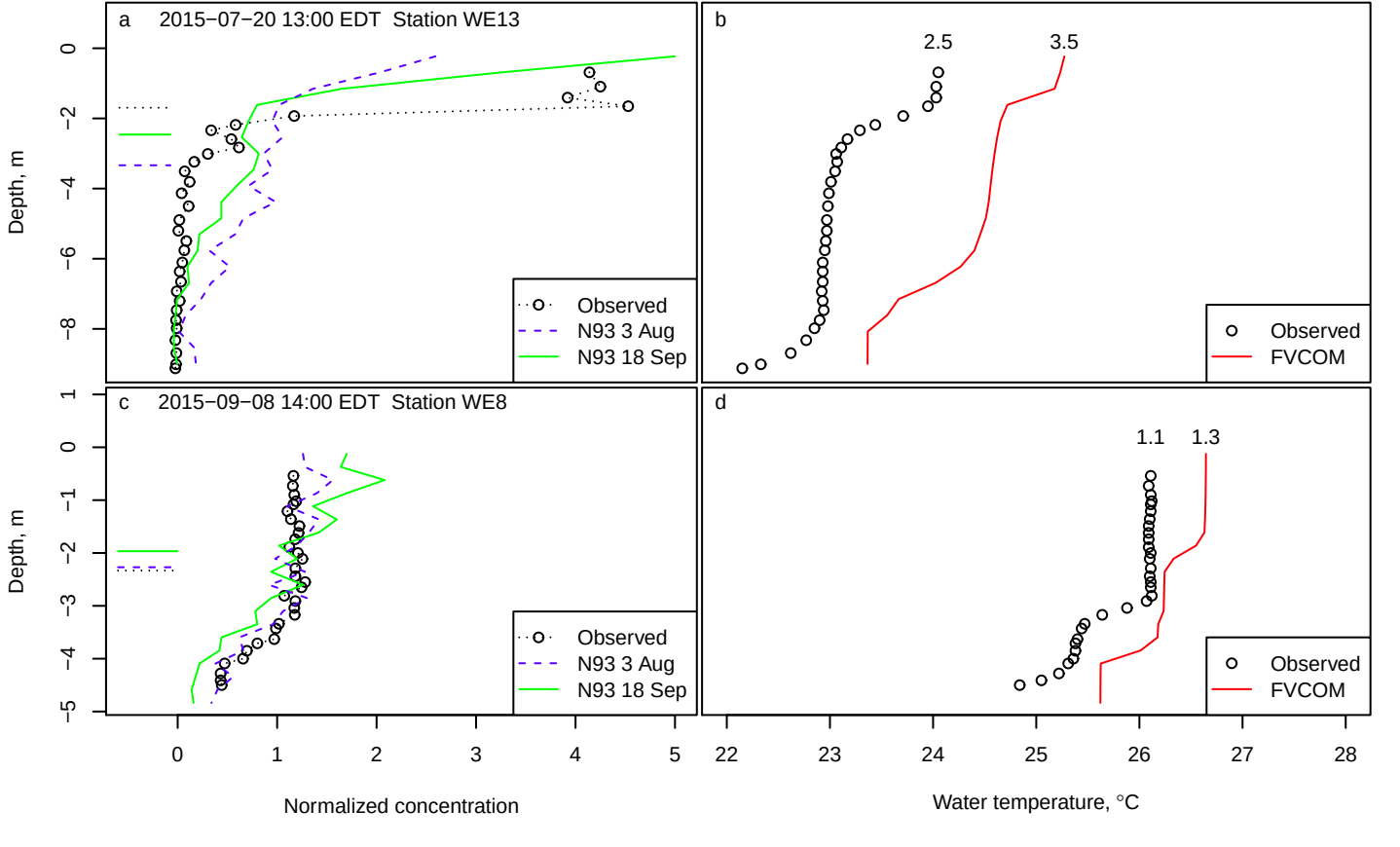
a 2015−07−20 13:00 EDT Station WE13
b
c 2015−09−08 14:00 EDT Station WE8
d
Depth, m
Depth, m
Normalized concentration
Water temperature, °C
Observed
N93 3 Aug
N93 18 Sep
Observed
FVCOM
2.5
3.5
1.1
1.3

Figure 6. Figure

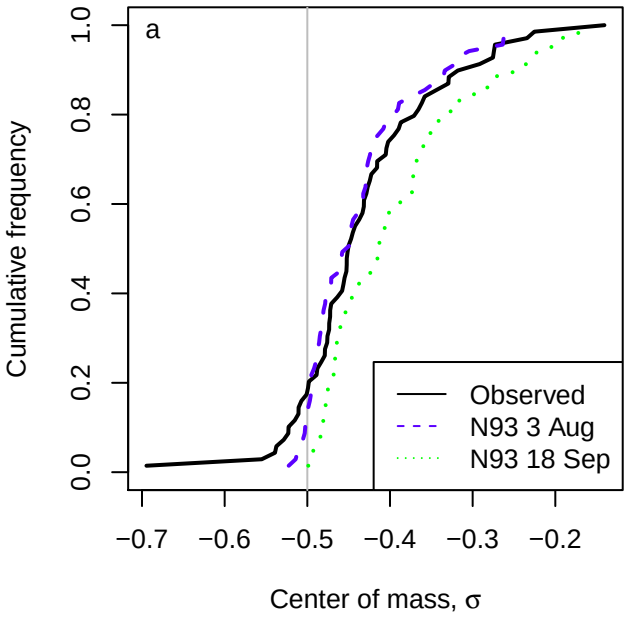
a
Cumulative frequency
0.0
0.2
0.4
0.6
0.8
1.0
−0.7
−0.6
−0.5
−0.4
−0.3
−0.2
Center of mass, σ
Observed
N93 3 Aug
N93 18 Sep

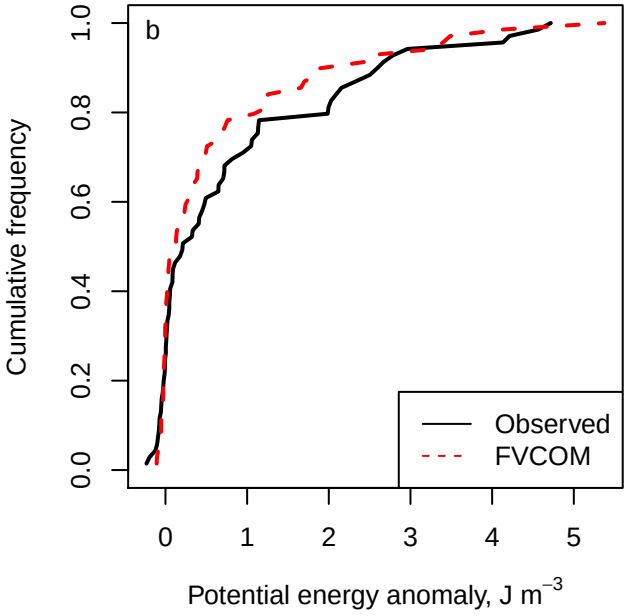
b
Cumulative frequency
0.0
0.2
0.4
0.6
0.8
1.0
0
1
2
3
4
5
Potential energy anomaly, J m^{-3}
Observed
FVCOM

Figure 7. Figure

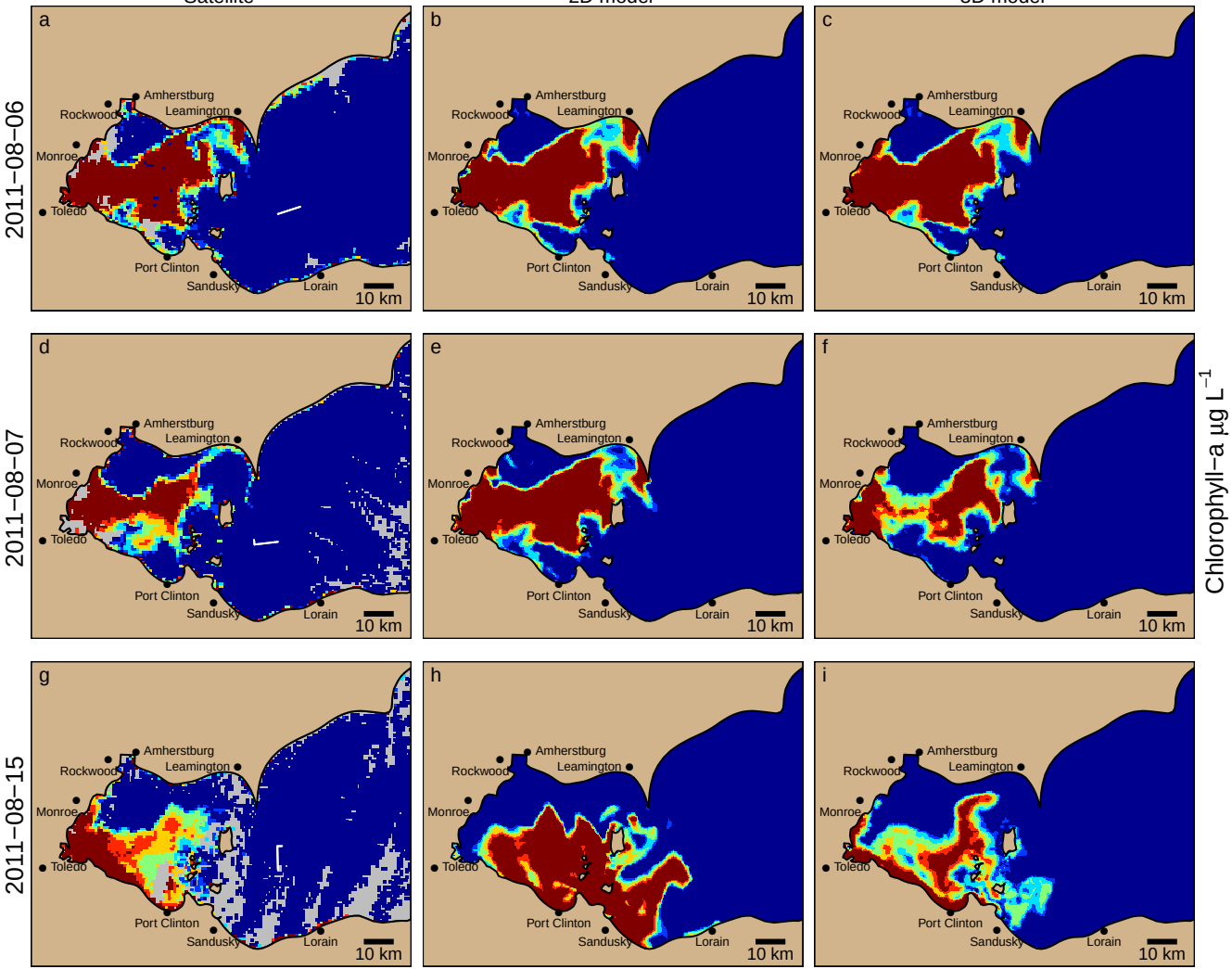
Satellite
2D model
3D model
2011−08−06
2011−08−07
2011−08−15
a
b
c
d
e
f
g
h
i
Amherstburg
Leamington
Rockwood
Monroe
Toledo
Port Clinton
Sandusky
Lorain
10 km
Chlorophyll−a µg L−1
100
80
60
40
30
23
0

Figure 8. Figure

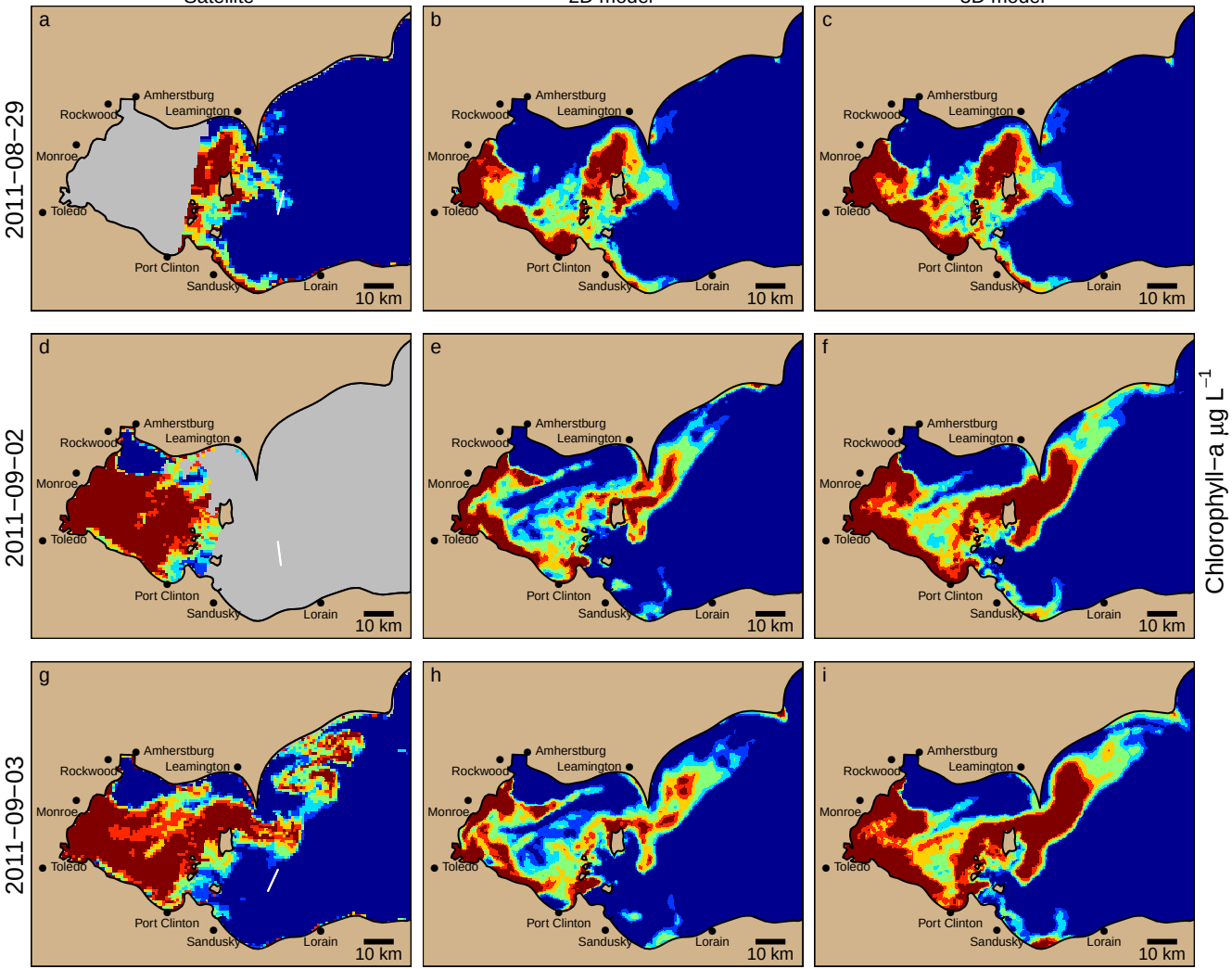
Satellite
2D model
3D model
2011−08−29
2011−09−02
2011−09−03
a
b
c
d
e
f
g
h
i
Amherstburg
Leamington
Rockwood
Monroe
Toledo
Port Clinton
Sandusky
Lorain
10 km
Chlorophyll−a µg L−1
100
80
60
40
30
23
0

Figure 9. Figure

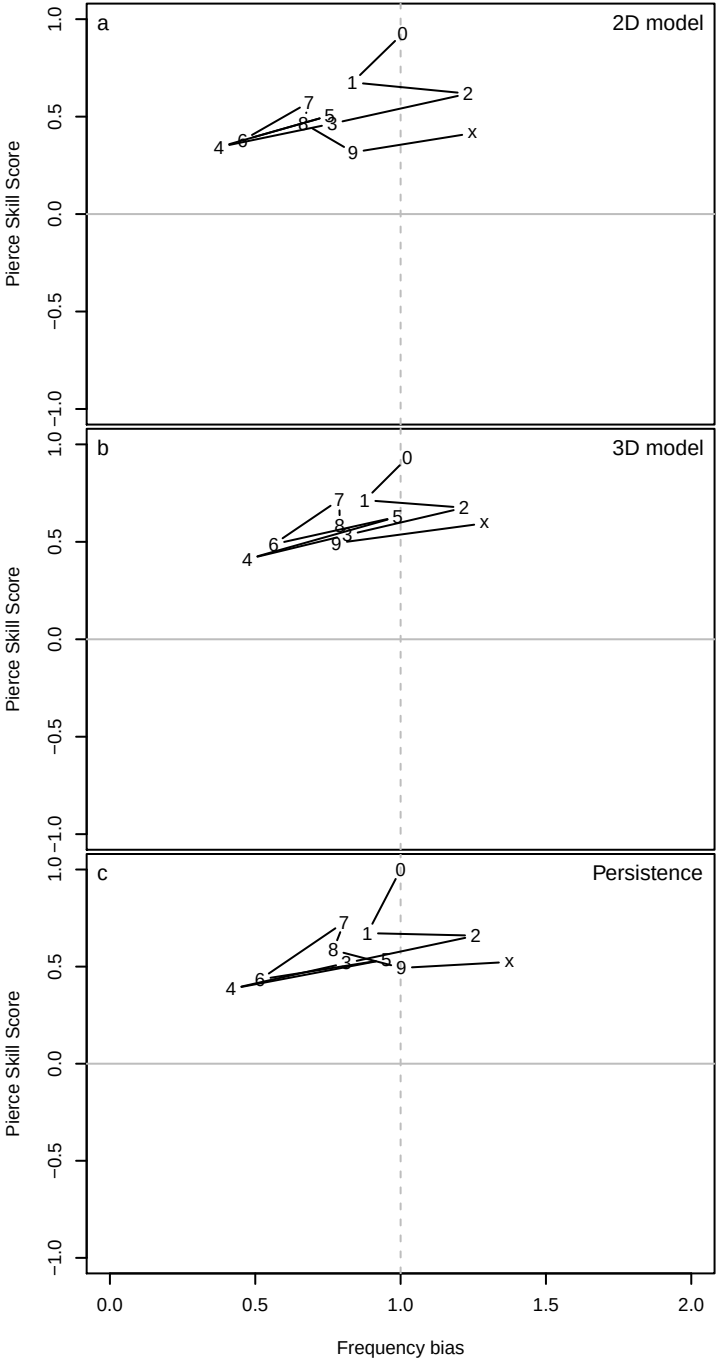
a
2D model
b
3D model
c
Persistence
Pierce Skill Score
Frequency bias
1.0
0.5
0.0
−0.5
−1.0
0.0
0.5
1.0
1.5
2.0
0
1
2
3
4
5
6
7
8
9
x

Figure 10. Figure

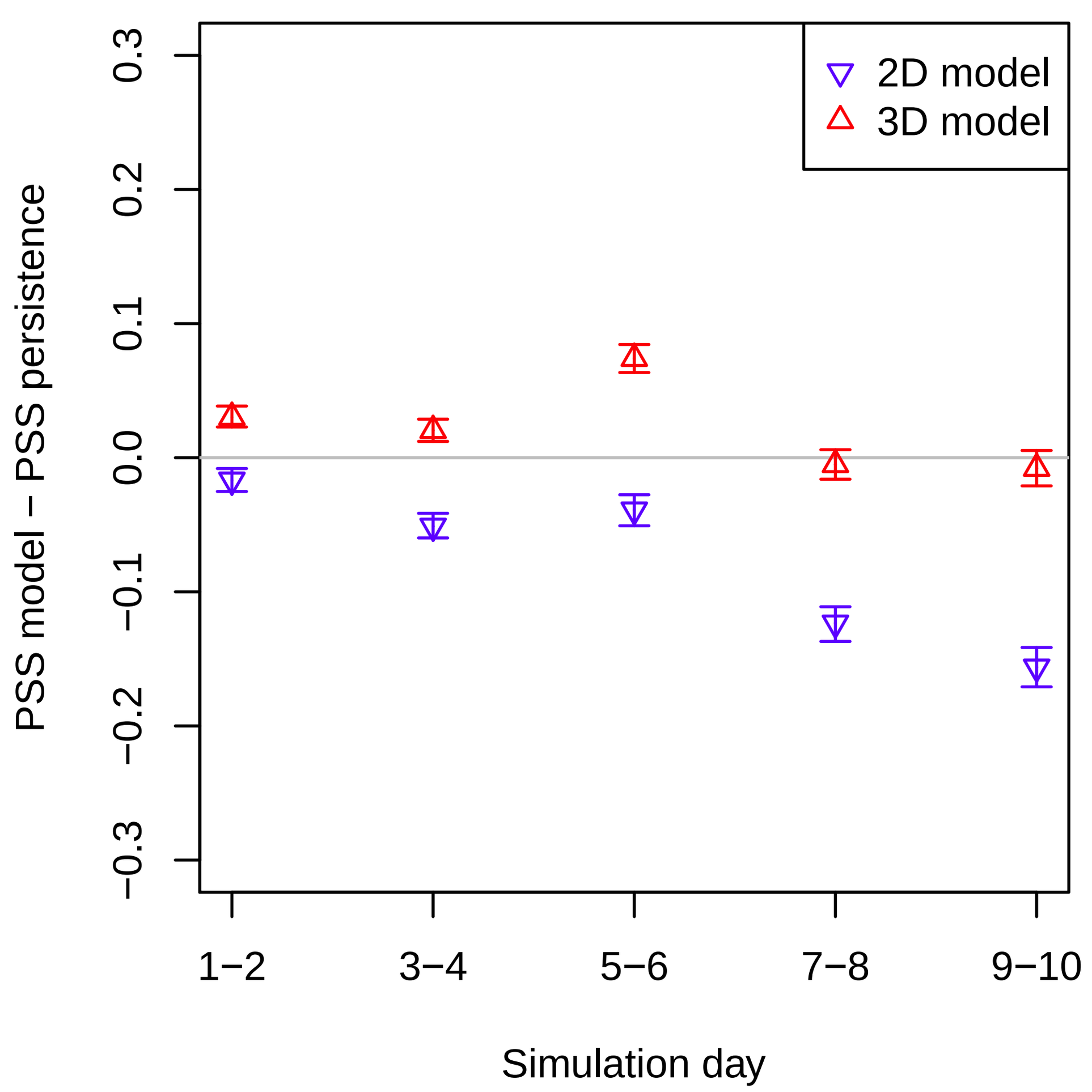
2D model
3D model
PSS model – PSS persistence
0.3
0.2
0.1
0.0
−0.1
−0.2
−0.3
1−2
3−4
5−6
7−8
9−10
Simulation day